nature reviews materials

https://doi.org/10.1038/s41578-024-00668-z

Review article

Check for updates

Nonlinear and quantum photonics using integrated optical materials

Avik Dutt [1,2,3,7] ✉, Aseema Mohanty [4,7], Alexander L. Gaeta [5,6] & Michal Lipson [6]

Abstract

Integrated nonlinear photonics provides transformative capabilities for controlling, enhancing and manipulating material nonlinearities in miniaturized on-chip platforms. The extreme reduction of optical mode areas within subwavelength waveguides allows for large enhancements of light–matter interactions resulting in nonlinear phenomena at significantly lower optical powers than their fibre and free-space counterparts. The integration of nonlinear materials into nanophotonics has been instrumental in the practical implementation of emerging applications such as quantum information processing, high-speed optical communications, ultraprecise frequency metrology and spectroscopy. Since the early 2000s, the development of new fabrication methods combined with nanoscale design has led to tremendous improvements in the quality and integration capability of both traditional and new nonlinear material platforms. In this Review, we outline design principles to harness the potential of nonlinear materials on integrated platforms through improvements in waveguide loss, resonator design and dispersion engineering principles. We discuss how these tools have been used towards realizing several of the major goals of integrated nonlinear photonics such as broadband frequency conversion, frequency-comb generation, quantum light sources and nonlinear optical quantum logic gates.

Sections

[1]Department of Mechanical Engineering, University of Maryland, College Park, MD, USA. [2]Institute for Physical Science and Technology, University of Maryland, College Park, MD, USA. [3]National Quantum Laboratory (QLab) at Maryland, College Park, MD, USA. [4]Department of Electrical and Computer Engineering, Tufts University, Medford, MA, USA. [5]Department of Applied Physics and Applied Mathematics, Columbia University, New York, NY, USA. [6]Department of Electrical Engineering, Columbia University, New York, NY, USA. [7]These authors contributed equally: Avik Dutt, Aseema Mohanty. ✉e-mail: avikdutt@umd.edu

Introduction

Nonlinear optics — the study of photon–photon interactions by way of materials — enables the all-optical control of light and the generation of new frequencies. Harnessing nonlinear optical phenomena using integrated photonics allows for unprecedented control and enhancement of material nonlinearities within a compact chip-scale platform. Integrated photonics rely on nanoscale light guiding structures to miniaturize optical mode areas to subwavelength scale. In contrast to their free-space or fibre-based counterparts, in which nonlinear optics is naturally associated with high optical intensities, the small mode volumes of integrated photonic structures allow for nonlinear phenomena at extremely low powers. Such a platform allows for the system-level integration of nonlinear photonics, necessary for the practical implementation of emerging applications such as quantum information processing (QIP), high-speed optical communications, ultraprecise frequency metrology and spectroscopy.

Since the turn of the century, tremendous progress in improving the quality and integration of traditional materials such as Si[1–6], $LiNbO_3$ (refs. 7,8), Si_3N_4 (refs. 9,10), silica[11,12] and AlGaAs[13], and in developing new material platforms such as diamond[14], SiC[15–17], GaN and AlN (Fig. 1), has been achieved. In addition, the hybrid integration of novel 2D materials with such traditional platforms is strongly pursued for their highly tunable optoelectronic properties[18–20]. Furthermore, the recent emphasis on QIP brings opportunities for nonlinear parametric processes to build and manipulate quantum sources of light[21,22] and even combine them[23–25] with microresonator frequency combs, which have experienced rapid progress[26–29].

In integrated photonics, high-confinement waveguides play a crucial role, enabling key design tools such as dispersion engineering[1,30], low-loss propagation[31–34] and strong field localization[35], which have become indispensable for harnessing the intrinsic nonlinearities of different material platforms. In this Review, we outline design principles and progress in using these tools to achieve major goals in integrated nonlinear photonics such as broadband frequency conversion, frequency-comb generation, quantum light sources and nonlinear optical quantum logic gates (Fig. 1). As an example, improvements in roughness at the core–cladding interface and in the film quality over the past 10 years have reduced the oscillation threshold for Kerr frequency combs from 50 mW to 20 μW since their first demonstrations[31,36–38], reducing the need for optical amplifiers[31]. We discuss trade-offs between design criteria for each application, keeping in mind fabrication considerations. We also discuss the current state of the art and improvements that are needed to achieve the desired figures of merit for each application.

Integrated nonlinear optics

The strong localization of light within waveguides enables the versatile engineering of its amplitude and phase, which are key to enhancing nonlinear optical processes. The high optical intensities provided by waveguides lead to consequential higher-order terms of the material polarization — enhancing photon–photon interactions and generating new frequencies. At optical frequencies, the response of dielectrics to electromagnetic radiation is governed by the source-free Maxwell's wave equations, with a material polarization term that can be expanded as a Taylor series of the electric field E in the electric dipole approximation:

$$\vec{P}^{(\mathrm{NL})} = \varepsilon_0\left[\underline{\chi}^{(1)} + \underline{\chi}^{(2)}\vec{E} + \underline{\chi}^{(3)}\vec{E}\,\vec{E} + \cdots\right]\vec{E}, \quad (1)$$

in which $\underline{\chi}$s are tensors of appropriate rank for the susceptibility and ε_0 is the permittivity of free space[39]. The first term — the linear response — is responsible for the linear refractive index (n_0): $n_0 = \sqrt{1+\chi^{(1)}}$. The second and third terms corresponding to the second-order ($\chi^{(2)}$) and third-order ($\chi^{(3)}$) nonlinearity govern wave mixing processes (Fig. 1a and Boxes 1 and 2). $\chi^{(2)}$ vanishes in materials that lack inversion symmetry (non-centrosymmetric), although electric quadrupole effects can give rise to second-order nonlinear processes in bulk centrosymmetric crystals[40]. $\chi^{(3)}$ can also produce a refractive index change that is quadratic in the input field E and linear in the intensity: $I \propto |E|^2$: $n = n_0 + n_2 I$, whereby the nonlinear index coefficient is $n_2 = 3\chi^{(3)}/4n_0^2 c\varepsilon_0$.

A key challenge has been incorporating $\chi^{(2)}$ materials on integrated photonics platforms as $\chi^{(2)}$ nonlinearity vanishes for all amorphous solids including most commonly used deposited thin films. Nevertheless, novel fabrication methods including epitaxial growth and bonding have been used to successfully integrate $\chi^{(2)}$ materials such as $LiNbO_3$ (LN), AlN, III–V and SiC[7,15,17,41,42]. Certain crystals made of more than one type of atom possess a non-vanishing $\chi^{(2)}$ (refs. 43,44). The design of photonic structures using these materials must account for crystal orientations and the polarization directions of the interacting fields to maximally utilize the non-zero components of their $\chi^{(2)}$ tensor. $\chi^{(2)}$ platforms enable unique functionalities such as ultra-broadband frequency conversion, pure phase (Pockels) modulators and parametric down conversion (PDC) quantum light sources. The rapid maturity of the field has been exemplified by the obtention of high-performance modulators in thin-film LN[7].

By contrast, $\chi^{(3)}$ nonlinearity is ubiquitous in all materials and, therefore, has been widely studied in silicon and, later, in Si_3N_4, Hydex, silica and other amorphous materials, leading to many four-wave mixing (FWM)-based applications. Examples include Kerr frequency-comb generation for spectroscopy and frequency metrology, supercontinuum generation and the generation of nonclassical states of light for quantum information science. For $\chi^{(3)}$ processes, all the interacting fields can be close in frequency, making the design of photonic structures easier. Note that we focus on parametric nonlinear processes in this Review, whereby the photon energy is conserved in the optical domain. We refer the reader to excellent other reviews on non-parametric processes such as Brillouin[45] and Raman scattering[46], which couple photons with phonons.

Another major challenge for integrated platforms is that the tight confinement of light within waveguides, which enhances nonlinear interactions, also increases the susceptibility to losses. Although silicon was a material of choice for chip-scale nonlinear platforms during the early development of integrated photonics[1], high linear losses, two-photon absorption (TPA) and TPA-induced free-carrier absorption (FCA) made it difficult to achieve high performance at near-infrared wavelengths. In particular, the indirect bandgap of silicon leads to long-lived free carriers that negatively affect performance compared with direct bandgap materials such as AlGaAs. This impaired performance has prompted substantial efforts to develop large bandgap materials such as silica, Si_3N_4, AlN and LN for nonlinear nanophotonics.

Although the efficiency of nonlinear processes typically increases with both interaction length L and optical power, linear and nonlinear losses set limits on the effective interaction lengths and powers, respectively, beyond which the efficiency stops increasing (Box 1). As opposed to linear loss, the deleterious effects of nonlinear loss mechanisms such as TPA become dominant at high powers, whereby two photons with energy more than half the bandgap are absorbed simultaneously.

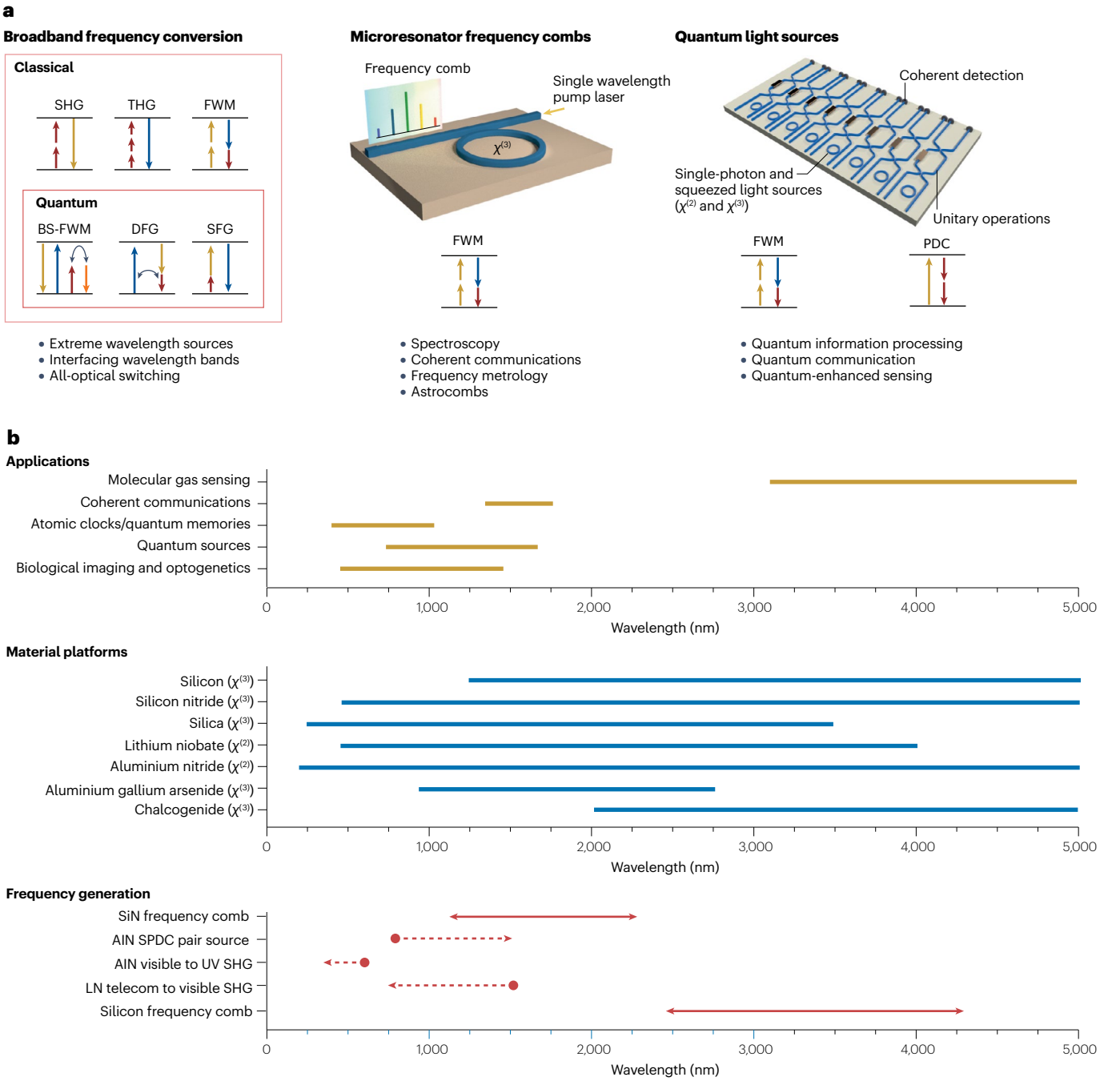

Fig. 1 | Overview of integrated nonlinear photonic material platforms and applications. a, Main goals of integrated nonlinear photonics and their corresponding nonlinear processes. **b**, Selected applications, nonlinear photonic material platform transparency windows and examples of frequency generation using nonlinear integrated photonics spanning the visible to mid-infrared spectrum[78,113,194,257,357]. DFG, difference frequency generation; FWM, four-wave mixing; BS-FWM, Bragg scattering four-wave mixing; LN, lithium niobate; PDC, parametric down conversion; SFG, sum-frequency generation; SHG, second-harmonic generation; SPDC, spontaneous parametric down conversion; THG, third-harmonic generation; UV, ultraviolet.

To quantify this effect, one can define the nonlinear figure-of-merit $\mathrm{FOM} = \mathrm{Re}[\chi^{(3)}]/\mathrm{Im}[\chi^{(3)}] = n_2/(\beta_{\mathrm{TPA}}\lambda)$ for $\chi^{(3)}$ materials in which $\beta_{\mathrm{TPA}} = 3\mathrm{Im}[\chi^{(3)}]/4\varepsilon_0 c\lambda n_0^2$ is the TPA coefficient[47]. The net loss for an intensity I can then be quantified as $\alpha_{\mathrm{total}} = \alpha_{\mathrm{linear}} + \beta_{\mathrm{TPA}} I$.

Integrated photonics provides three key design tools to enhance optical nonlinearities: high-confinement waveguides, low-loss resonators and waveguide dispersion engineering (Box 3). Although the intrinsic material properties $\chi^{(2)}$ and $\chi^{(3)}$ are generally small, the fact

Box 1

Nonlinear parametric processes for wave mixing

Every parametric nonlinear process involves the interaction of waves at one or more frequencies to produce new waves in an energy-conserving manner. Representative examples of such processes are shown in the figure, in which dashed arrows indicate output fields and solid arrows indicate input fields. Among second-order $\chi^{(2)}$ nonlinear process, second-harmonic generation (SHG, $\omega = \omega \rightarrow 2\omega$) produces light waves at twice the incident light frequency, whereas sum-frequency generation (SFG) produces waves at frequency $\omega_{out} = \omega_{in1} + \omega_{in2}$ for input waves at $\omega_{in1,in2}$, respectively. The reverse of these two processes is parametric down conversion (PDC, $\omega_{in} \rightarrow \omega_{out1} + \omega_{out2}$). Difference frequency generation (DFG, $\omega_{in1} - \omega_{in2} \rightarrow \omega_{out}$), by contrast, can produce optical parametric amplification (OPA), or parametric gain, because this can be used to amplify the lower frequency waves. When this process is placed within an optical cavity for resonant enhancement, this is referred to as an optical parametric oscillator.

Among processes based on the third-order or Kerr nonlinearity $\chi^{(3)}$, a simple example is THG ($\omega + \omega + \omega \rightarrow 3\omega$). More generally, four-wave mixing (FWM, $\omega_{p1} + \omega_{p2} \rightarrow \omega_s + \omega_i$) generates a signal (s) and an idler (i) wave from two pump frequencies (p1, p2). Degenerate FWM in which the two pumps have the same frequency is commonly used to induce parametric gain, essential for generating Kerr frequency combs. In addition, $\chi^{(3)}$ processes lead to an intensity-dependent refractive index $n = n_0 + n_2 I$ to produce the optical Kerr effect, which leads to self-phase modulation (involving four identical frequencies, $\omega_{p1} = \omega_{p2} = \omega_s = \omega_i$) and cross-phase modulation (involving two pairs of identical frequencies, $\omega_{p1} = \omega_s \neq \omega_{p2} = \omega_i$). Here, the nonlinear index is $n_2 = 3\chi^{(3)}/4\varepsilon_0 c n_0^2$, in which n_0 is the linear index. FWM can lead to modulational instability or phase-conjugation FWM accompanied by parametric gain, whereby two pump photons are annihilated in pairs to generate a signal and an idler photon in pairs, producing quantum light sources in the process. Alternatively, FWM can lead to Bragg scattering (BS-FWM), whereby for each idler output photon that is created, one signal input photon is annihilated, enabling quantum frequency conversion. Note that all processes except self-phase modulation and cross-phase modulation can be used for classical frequency conversion — see the figure, in which the thickness of the arrows qualitatively depicts the relative intensities of the fields used in each process. In the figure, we emphasize especially those processes that can enable quantum frequency conversion,

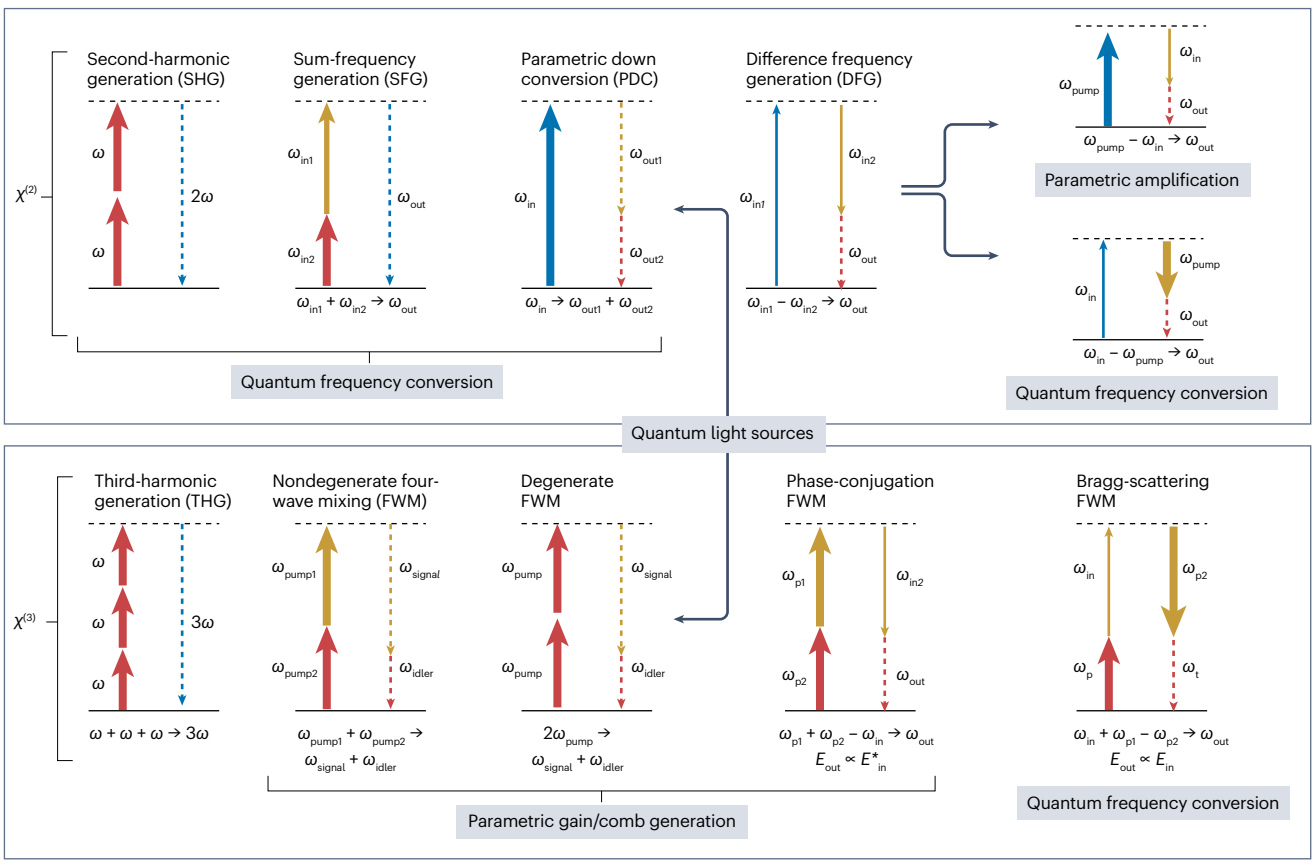

(continued from previous page)
frequency-comb generation, parametric gain/amplification and the generation of quantum light sources.

We next describe basics of a frequency comb — a prime application of nonlinear microresonators seeded by the aforementioned modulational instability FWM. An optical frequency comb consists of a series of narrow spectral lines that are equidistant in frequency and have a well-defined phase relationship, with line (or 'tooth') frequencies represented by:

$$f_n = f_{ceo} + mf_{rep}, \quad (6)$$

in which m is an integer, f_{rep} is the repetition rate equal to the spacing between adjacent 'tooth' of the comb and f_{ceo} is an overall frequency shift (carrier-envelope offset). A broad octave-spanning bandwidth is particularly necessary for f–$2f$ or $2f$–$3f$ interferometry to enable a fully self-referenced comb with precisely known frequencies[368] (equation (4)). Other key metrics include the threshold power for FWM parametric oscillation for comb generation, which is the input pump power P_{in} above which generated signal and idler modes experience parametric gain exceeding roundtrip loss and start oscillating, which can be written as[14,190]:

$$P_{th} \approx 1.54 \frac{\pi}{2} \frac{Q_C}{2Q_L} \frac{n_0^2}{n_2 \lambda_p} \left(\frac{V}{Q_L^2}\right) \sim \left(\frac{V}{Q_L^2}\right), \quad (7)$$

in which λ_p is the pump wavelength, $V \approx 2\pi R A_{eff}$ is the microresonator mode volume and Q_c and Q_L are the coupling quality factor and the loaded quality factor arising from the rate of ring–bus–waveguide coupling and the total loss rate, respectively.

Parametric nonlinear processes occur in materials, which possess purely real susceptibility tensor χ. In materials with complex nonlinear susceptibilities, the final quantum state of the system is no longer guaranteed to be identical, and thus the resulting process is non-parametric. The imaginary parts of the nonlinear susceptibilities can either lead to linear loss ($\alpha_{linear} = 2\pi \mathrm{Im}[\chi^{(1)}]/\lambda n_0$) and nonlinear loss mechanisms such as two-photon absorption or otherwise affect the efficiency of the parametric process.

that the dimensions of structures are on the same length scale as the wavelength leads to strong enhancement of the field, which, in turn, leads to strong nonlinear optical phenomena. Similarly, a strong linear material dispersion that would preclude satisfying phase-matching conditions in bulk can be markedly changed by tailoring fundamental and higher-order modes.

Material platforms for integrated nonlinear photonics

Silicon and group IV materials (or complementary metal–oxide–semiconductor-compatible)

Crystalline silicon (c-Si) has been the material of choice for integrated photonics since the early 2000s, driven by the need for high-bandwidth optical communication links. The massive infrastructure of the electronic semiconductor fabrication industry can be harnessed to produce silicon photonic devices at high yields and low cost and allows the integration of photonics and electronics on the same chip. The index of silicon (n ~ 3.5) is substantially higher than that of silicon dioxide (n ~ 1.45), making compact devices possible using a thin-film silicon core, based on silicon-on-insulator wafers commonly used in complementary metal–oxide–semiconductor (CMOS) foundries. Silicon modulators exploit the carrier-based plasma dispersion effect for active tunability and modulation. The bandgap of c-Si is 1.1 eV, which provides an optical transparency window from 1.2 μm to 8 μm. Silicon is a centrosymmetric material with a high $n_2 \sim 4 \times 10^{-18} m^2\,W^{-1}$. However, TPA and FCA have limited its use for many nonlinear optical applications in the near-infrared. High-confinement resonators with quality factors up to 1 million have been achieved for nonlinear mid-infrared applications[48]. TPA is absent in c-Si beyond 2.2 μm, and FCA can be mitigated using reverse-biased p–i–n junctions to actively extract carriers. By leveraging these features, c-Si has been utilized for nonlinear applications such as comb generation in the mid-infrared[2] and for quantum light sources in the near-infrared[49]. However, higher-order absorption processes still occur and limit optical power.

The field of silicon photonics today not only involves crystalline silicon but also many other silicon-based amorphous materials such as silicon nitride, silicon oxynitride, amorphous silicon (a-Si) and Hydex. Amorphous materials have a unique advantage because they can generally be deposited on various substrates using several techniques. Specifically, plasma-enhanced chemical vapour deposition can be operated at a low temperature of ~400 °C and is already part of CMOS foundry process flows, whereas low-pressure chemical vapour deposition at higher temperatures typically yields purer films with lower loss. Compared with crystalline Si, amorphous materials have lower absorption and scattering losses owing to a lower-index contrast with the cladding materials, but they possess lower linear and nonlinear indices. Tremendous effort in the photonics community has aimed to reduce losses in silicon nitride waveguides by reducing the impurities of the deposited film and its surface roughness to subatomic levels (<0.1 nm) through optimized etching and lithography, resulting in high-quality factors (Qs) greater than 70 million[31–33,50,51] (Fig. 2). Progress towards overcoming film stress has enabled the obtention of thicker films of silicon nitride without cracks, which satisfy the anomalous waveguide dispersion conditions needed for broadband frequency-comb generation[52–54]. By varying the composition, silicon-rich nitride also has the added benefit of a higher n_2 (refs. 55,56). However, the linear losses are increased and careful consideration must be taken during annealing (which is typically used to reduce losses) to avoid the formation of silicon clusters as a by-product. Owing to its larger bandgap of 1.7 eV, a-Si is less affected by TPA and FCA at telecom wavelengths (1.55 μm), despite possessing an n_2 that is several times higher than crystalline silicon[57–61].

Besides elemental Si, several other group-IV-based materials such as germanium, silicon carbide and diamond have garnered interest for their unique transparency windows. For instance, diamond[14] and silicon carbide[17] have very wide bandgaps (5.47 eV and 2.4–3.2 eV, respectively) and are useful for applications down to the visible and ultraviolet, whereas germanium has a narrow bandgap and is useful for light detection at telecommunication wavelengths. Germanium also has a high refractive index (~4) and correspondingly shows promise for efficient nonlinear optical processes into the mid-infrared as its

Box 2

Phase matching for nonlinear parametric processes

For a phase-matched process, energy conservation and momentum conservation are simultaneously satisfied. Thus, the waves created at new frequencies by the nonlinear interaction add up constructively, resulting in large output at the new frequencies. Consider a $\chi^{(2)}$ -based three-wave mixing process ($\omega_1 + \omega_2 = \omega_3$), for which the phase mismatch is

$$\Delta\beta = \beta(\omega_1) + \beta(\omega_2) - \beta(\omega_3) = \frac{1}{c}\left(\frac{n(\omega_1)}{\omega_1} + \frac{n(\omega_2)}{\omega_2} - \frac{n(\omega_3)}{\omega_3}\right),$$

in which $n(\omega)$ and $\beta(\omega)$ are, respectively, the effective refractive index and propagation constant of the mode at frequency ω. In the case of second-harmonic generation and degenerate parametric down conversion ($\omega_1 = \omega_2 = \omega_3/2 = \omega$), the phase-matching condition $\Delta\beta = 0$ simplifies to $n(\omega) = n(2\omega)$. Away from the ideal phase-matching condition $\Delta\beta \neq 0$, the conversion efficiency in a propagation medium of length L degrades as $\sin c^2(\Delta\beta L/2)$.

For $\chi^{(3)}$-based four-wave mixing (FWM) processes, self-phase modulation (SPM) and cross-phase modulation (XPM) play important roles in phase matching (Box 1). The phase-matching condition for third-harmonic generation is similar to second-harmonic generation: $n(\omega) = n(3\omega)$. More generally, a FWM process $\omega_{p1} + \omega_{p2} \rightarrow \omega_s + \omega_i$ with two intense pumps at $\omega_{p1,p2}$ with powers $P_{1,2}$ has a net phase mismatch[144]:

$$\Delta\beta(P_1, P_2) = [\beta(\omega_s) + \beta(\omega_i) - \beta(\omega_{p1}) - \beta(\omega_{p2})] + \gamma(P_1 + P_2)$$
$$\approx \beta_2 \times [(\omega_s - \omega_i)^2 - (\omega_{p1} - \omega_{p2})^2] + \gamma(P_1 + P_2),$$

in which the first term represents the linear wavevector mismatch and the last term represents the contribution from SPM and XPM. $\beta_2 = d^2\beta(\omega)/d\omega^2$ is the group-velocity dispersion (GVD) at the average pump frequency $(\omega_{p1} + \omega_{p2})/2$. For the commonly used case of degenerate pumps $\omega_{p1} = \omega_{p2}$ and $P_1 = P_2 = P_0$, the net phase mismatch reduces to $\Delta\beta \approx \beta_2 \times (\omega_s - \omega_i)^2 + 2\gamma P_0$. Most materials have a positive Kerr nonlinearity $\gamma = \omega n_2/cA_{eff} > 0$. Thus, to compensate for SPM-induced and XPM-induced phase shifts and ensure $\Delta\beta \approx 0$, we require $\beta_2 < 0$, that is, anomalous GVD at the pump wavelength.

The figure shows typical effective index (n_{eff}) variation of a waveguide mode with wavelength λ (dispersion exaggerated for clarity). High-index-contrast systems show large λ-dependent spatial mode variation, allowing n_{eff} and the consequent GVD to be changed

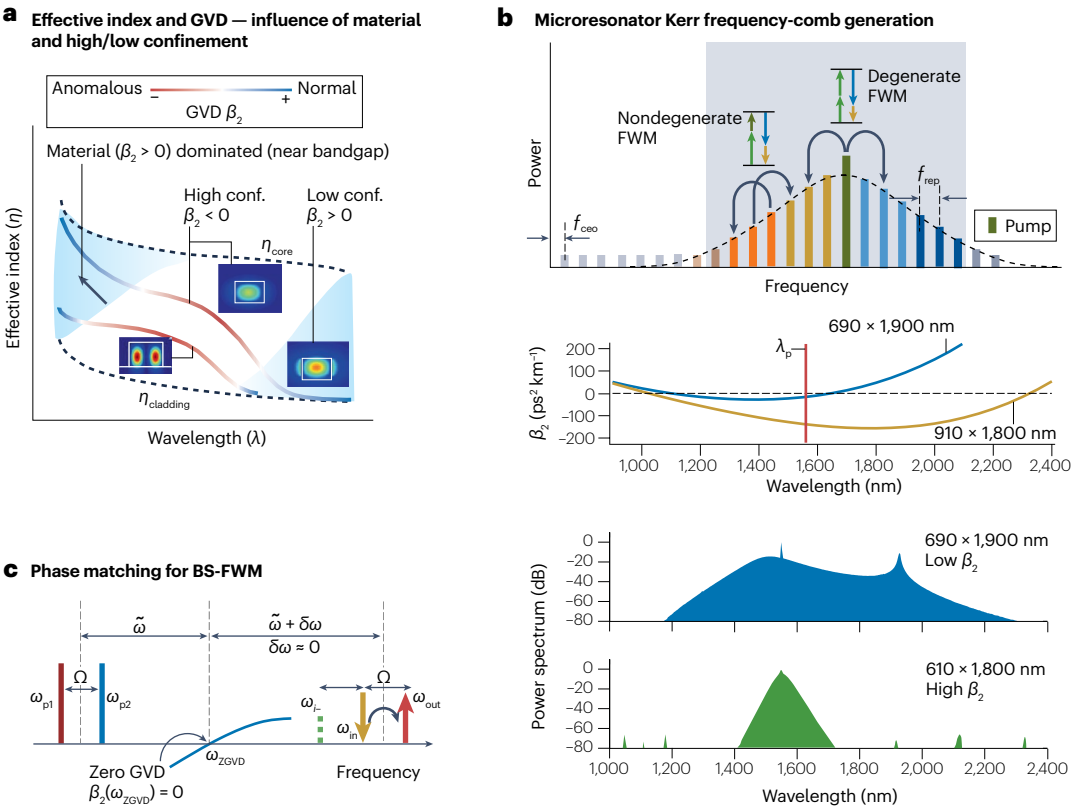

ceo, carrier-envelope offset; rep, repetition. Part **b** reprinted with permission from ref. 210, Optica.

(continued from previous page)
from being normal in the low-confinement (large λ) limit to possibly anomalous in the high-confinement regime. At lower λ close to the bandgap, the material dispersion becomes strongly normal, and higher-order modes can extend the range of wavelengths possessing anomalous GVD.

A phase-matched FWM process can produce parametric gain and modulational instability (important for frequency-comb generation, see the figure) and also produce phase-conjugated idlers. Microresonator Kerr frequency-comb generation involves degenerate and non-degenerate FWM at the initial stages. These processes are phase-matched for a low anomalous GVD. As shown in the bottom of panel **b**[210], a low negative β_2 results in a broader comb than a high β_2.

If the pumps and input/output frequencies are instead chosen to satisfy $\omega_{p1} + \omega_{in} \rightarrow \omega_{p2} + \omega_{out}$, the phase mismatch is modified to

$$\Delta\beta(P_1, P_2) \approx \beta_2 \times (\omega_{p2} - \omega_{p1})(\omega_{p2} - \omega_{in})/2 + \gamma(P_1 - P_2)/2.$$

Note that the SPM/XPM contribution from the two pumps can be cancelled by equal pump powers ($P_1 = P_2$). The aforementioned process, called Bragg scattering FWM (BS-FWM) (Box 1), is phase-matched when the average frequency of the four waves coincides with the zero GVD (ZGVD) frequency: $\omega_{ZGVD} = (\omega_{p1} + \omega_{in})/2 = (\omega_{P2} + \omega_{out})/2$, as $\beta_2(\omega_{ZGVD}) = 0$ (see the figure, panel **c**). In other words, phase matching in BS-FWM requires the pump fields and the input/output fields to be placed symmetrically about the zero-GVD point ω_{ZGVD}. In the figure, panel **c**, we also indicate ω_{i-} as the spurious lower sideband BS-FWM idler, which is also phase-matched to the lowest order. Contributions from higher-order dispersion can modify phase-matching conditions for widely separate pumps and signal-idler beams, both for BS-FWM[21,142] (equation (3)) and for phase conjugation and/or modulational instability FWM[209,210].

transparency window extends to 14 μm (ref. 62). Of these materials, germanium can be epitaxially grown on top of silicon and has been used for integrated near-infrared detectors in foundry-level photonics. SiGe has also been used for ultrabroadband supercontinuum generation up to the mid-infrared[63,64]. Integrating SiC and diamond remained a challenge for a long time because SiC-on-oxide and diamond-on-oxide thin films were not widely available and were difficult to etch[17,65–67], but these fabrication challenges have since been addressed[15,16,68–70].

III–V materials

Crystalline materials based on III–V compound semiconductors (InGaP, InP, GaP, GaAs and derivatives and III-nitrides) are typically direct bandgap materials and have high refractive indices, enabling lasers and amplifiers to be fabricated on the same platform as photonic integrated circuits. III–V materials such as aluminium nitride, GaP and GaAs are also non-centrosymmetric, and several materials in this class possess the largest second-order nonlinearities for crystalline dielectrics ($\chi^{(2)} >$ ~150 pm V^{-1} for GaP, InAs and GaAs). By changing the material composition (such as the ratio of Al and Ga in $Al_xGa_{1-x}As$), the bandgap and thus the transparency window can be easily tuned to prevent TPA. III–V thin films can be incorporated on silicon wafers through wafer bonding and direct growth techniques[71,72]. AlGaAs was initially proposed in the 1990s as one of the first platforms for integrated nonlinear optics and, in particular, has the advantage of lower TPA and FCA in the C-band for Al content higher than 0.3 owing to its electronic band structure[73–75]. However, only after the development of the AlGaAs-on-insulator platform, which enables high-confinement structures, was it possible to generate Kerr frequency combs in this material[13,76]. Epitaxially grown crystalline AlN on sapphire has the highest bandgap of any integrated material with a large $\chi^{(2)}$ leading to high quality factors of 200,000 in the ultraviolet wavelength range[77,78] (Fig. 2b). By contrast, sputter-deposited polycrystalline AlN is more accessible commercially, although nonlinear $\chi^{(2)}$ processes are not as efficient as in crystalline AlN because of the mismatch in crystal orientation between different crystal grains[79]. The wide transparency range of AlN has enabled the obtention of frequency combs and classical and/or quantum frequency conversion (QFC) outside the telecommunication wavelength range[43,80–82].

Lithium niobate ($LiNbO_3$)

Lithium niobate (LN) is a well-known nonlinear material with a substantial $\chi^{(2)} = 27$ pm V^{-1}. Because thin-film LN-on-oxide is now commercially available[83], low propagation loss, high-confinement LN-on-insulator has been developed, opening the door to the development of highly compact, ultra-high-speed electro-optic modulators. High-confinement LN represents an impactful advance as it is a near-ideal platform with low loss (Q ~ 10 million) and important second-order and third-order nonlinearities[83] (Fig. 2b), which makes it attractive for several applications. Bulk LN is often doped with MgO to increase its power-handling capacity and mitigate photorefractive damage effects, which can also be done on integrated platforms. Techniques to mitigate the photorefractive effect on integrated platforms include removing the dielectric cladding layers and heat treatment[84].

Silica glasses and chalcogenides

Silica has been widely used as a traditional optical material owing to its substantially lower losses and was perfected for long-haul telecommunications over fibres. However, the low index of silica (1.45) means that cladded silica waveguides need to be several wavelengths (~10 μm) in cross-sectional dimensions. An alternative way to achieve high confinement uses air-clad suspended structures, but such structures are not fully integrated on chip. Advances have combined ultra-high Q silica resonators with planar silicon nitride waveguides[11]. Silica microresonators have good nonlinear performance owing to record-high Qs of 875 million[85]. High-index doped glass, or Hydex, is another alternative that enables the obtention of relatively high-confinement planar structures. Chalcogenides such as As_2S_3 and As_2Se_3 have shown promise, especially in the mid-infrared, owing to their high index and extremely high nonlinear coefficients. Although the photosensitivity of chalcogenides can be an issue, this feature has also been used for post-trimming to compensate for fabrication imperfections[86].

Organic polymers and emerging ferroelectrics

Organic polymers and emerging ferroelectrics such as lead zirconate titanate (PZT) and barium titanate ($BaTiO_3$ or BTO) exhibit the highest bulk optical nonlinearities owing to their unique molecular or crystalline structures[87–90]. Their $\chi^{(2)}$ is an order of magnitude above that of LN, with crystalline tetragonal BTO exhibiting the largest Pockels coefficient

Box 3

Integrated photonic design tools

High-confinement waveguides

High-confinement waveguides allow one to confine light into subwavelength cross-sectional areas, which give two key advantages: high optical intensity with lower input optical powers and diffraction-free propagation for increased interaction length within the nonlinear material. The degree of confinement increases with the linear refractive index contrast between the core and the cladding material. This is reflected in a small effective interaction area A_{eff} (four-wave mixing process) defined as:

$$A_{\mathrm{eff}}^{-1} = \frac{\int E_i^* E_j^* E_k E_l \mathrm{d}A}{\prod_i \left(\int |E_i|^2 \mathrm{d}A\right)^{1/2}},$$

in which E is the electric field. Values of A_{eff} are approximately on the order of $\left(\frac{\lambda}{n_0}\right)^2$. Empirical guidelines for film thicknesses and waveguide widths (w) that lead to optimal nonlinearity through small mode areas were derived by Foster et al.[369], as the mode area increases rapidly for waveguide dimensions $w \ll \lambda/n_0$ and linearly for $w \gg \lambda/n_0$.

As an example, self-phase modulation (or Kerr-phase shift) introduced by a beam of power P over an interaction length L is $\phi_{\mathrm{NL}} = \gamma PL$, and the nonlinear parameter γ is defined as:

$$\gamma = \frac{n_2 \omega}{c A_{\mathrm{eff}}},$$

in which $n_2 = \frac{3\chi^{(3)}}{4 n_0^2 \varepsilon_0 c}$ is the nonlinear index, n_o is the linear refractive index, ω is the frequency, c is the speed of light and A_{eff} is the effective mode area. The nonlinear parameter captures the effect of tight confinement (small A_{eff}) and a large n_2 and shows that large values of γ can achieve the same nonlinear phase shift (and other $\chi^{(3)}$ processes) with lower powers over a shorter length[370]. Compared with fibres ($\gamma \sim 10^{-3} - 10^{-2}\,\mathrm{W^{-1}m^{-1}}$), chip-scale waveguides can achieve nonlinear parameters ($\gamma \sim 1 - 1{,}000\,\mathrm{W^{-1}m^{-1}}$), with highest reported values in AlGaAs[371] (>500 $\mathrm{W^{-1}m^{-1}}$) and amorphous silicon (>700 $\mathrm{W^{-1}m^{-1}}$)[370,372]. Propagation in high-confinement waveguides can be as long as 0.4 m in an 8-$\mathrm{mm^2}$ footprint[170].

Low-loss resonators

Ultra-low-loss cavities have markedly increased intensities on-chip allowing for efficient nonlinear interaction between modes at different resonant frequencies using submilliwatt continuous-wave lasers. The resonant power enhancement within a cavity is governed by the following parameters:

$$\frac{P_{\mathrm{cav}}}{P_{\mathrm{in}}} = \frac{\lambda}{\pi^2 R n_{\mathrm{eff}}} Q_c \left(1 + \frac{Q_c}{Q_i}\right)^{-2} \left(\sim \frac{F}{\pi} \text{ for critical coupling } Q_c = Q_i\right)$$

in which $Q_{i/c}$ are the intrinsic and coupling quality factor dependent on intrinsic and extrinsic cavity loss rates owing to internal absorption and scattering losses and coupling to the bus waveguide, R is the resonator radius, n_{eff} is the effective index of the waveguide and $F = \frac{\lambda^* Q}{2\pi R n_{\mathrm{eff}}}$ is the finesse of the cavity, proportional to the number of roundtrips taken by the light. The highest optical power that can be realized within the cavity occurs under the critical coupling condition when the extrinsic and intrinsic losses are the same ($Q_c = Q_i$). For a number of applications, critical coupling is not optimal. For example, overcoupled cavities ($Q_c < Q_i$) are important for Bragg scattering-four-wave mixing frequency conversion in a ring[139], for efficient pump-to-comb conversion[216,362] and for squeezed-light generation[249,309], whereas undercoupled cavities ($Q_c > Q_i$) are important for low threshold in comb generation and in parametric oscillation[31,191].

Waveguide dispersion engineering

Integrated optics has greatly expanded the capabilities of achieving phase matching for efficient nonlinear processes through control of device geometry, which enables photonic structure dispersion to overcome the intrinsic dispersion of a material. Difficult phase-matching conditions can be achieved by the effective index of the waveguide modes, often belonging to different transverse orders, instead of the bulk material index (Box 2 and Fig. 3d). Phase-matching techniques specific to high-index-contrast platforms include engineering the cross-sectional dimensions[373] in single-mode or few-mode waveguides and the use of higher-order transverse modes in multimode waveguides[221,257]. Small geometry changes in high-confinement waveguides alter the field distribution significantly (Fig. 3a), resulting in a wavelength-dependent n_{eff} and large changes in group-velocity dispersion (GVD). For visible wavelengths, the dispersion provided by higher-order transverse modes is often necessary to compensate the extremely large normal GVD of the material close to their bandgap[221,374] (Box 2 and Fig. 3b).

Dispersion-engineered waveguides often require dimensions that support many modes, although only the fundamental mode is utilized. The fundamental mode can have avoided mode crossings with higher-order spatial or polarization modes[375], which cause large narrowband changes in dispersion that are harmful, for example, for broadband soliton microcomb generation. Avoided mode crossings can be mitigated by introducing tapered single-mode filtering regions or can be harnessed for local anomalous dispersion control in otherwise normal dispersion structures. Beyond single-waveguide geometries, the past few years have witnessed further dispersion engineering using more complex geometries, such as coupled waveguides[376], the use of thin films of a different material[211,212,377] or coupled resonators[363,378] and arrays[282] (Fig. 4a,b).

Quasi-phase-matching techniques of periodic poling that are traditionally used in low-index-contrast systems have been introduced into high-index-contrast nanophotonic platforms[44,107] and are expected to have an important role in $\chi^{(2)}$-based frequency conversion and in quantum light sources (Fig. 4c). Here, the direction of crystal orientation is periodically reversed by applying a strong electric field, with a period determined by the coherence length $L_{\mathrm{coh}} = \pi/\Delta\beta$, so the generated waves from successive periods add constructively despite the phase mismatch $\Delta\beta$. Additionally,

(continued from previous page)
wavelength-scale structures such as photonic crystals can engineer GVD by perturbing a single azimuthal mode of a ring resonator[379–381] (Fig. 3b) or lead to phase-matched nonlinear processes in standing-wave resonators (unlike travelling-wave ring resonators) with small mode volumes[51,382]. Finally, extreme subwavelength structures such as metasurfaces (Fig. 4d) can relax phase-matching requirements because the nonlinear interaction happens over a short propagation length $L \ll L_{coh}$.

of r_{42} = 923 pm V^{-1} (ref. 90). Organic polymers and PZT can be solution processed on top of more traditional photonic platforms to create hybrid waveguides in which light interacts strongly with the nonlinear material. BTO can be epitaxially grown on silicon and silicon dioxide on a wafer scale, making it highly attractive. In contrast to the organic materials, PZT and BTO can sustain higher temperatures. Studies into the thermal and chemical stability of these materials are ongoing.

Two-dimensional materials

Two-dimensional materials consist of a single atomic layer that confines electrons in one dimension leading to strongly tunable optoelectronic properties. Because 2D materials bond via van der Waals interactions to other surfaces, they can be transferred onto most substrates without limitations of lattice matching. This enables the addition of the nonlinear optical functionality inherent to 2D materials to traditional photonic platforms such as silicon and silicon nitride. Graphene was the first 2D material to be studied in electronics and the first monolayer whose optical properties were investigated. Owing to its inversion symmetry, nonlinear optical studies were limited to $\chi^{(3)}$ properties such as third-harmonic generation (THG) and FWM[19,91–93]. Graphene was soon followed by transition metal dichalcogenides (TMDs), which, unlike graphene, possess a bandgap, thus offering more versatility and lower loss. TMDs lack inversion symmetry when they consist of an odd number of layers, so monolayer TMDs exhibit a strong $\chi^{(2)}$. TMDs have strong excitonic effects and could potentially lead to high-temperature Bose–Einstein condensation, which is a signature of strong nonlinearity owing to interactions between excitons[94].

An important challenge to the widespread adoption of 2D materials is the growth of high-quality monolayers over large areas (approximately centimetre scale) with a low density of defects and grain boundaries and their reliable transfer to photonic platforms. In this respect, graphene oxide has emerged as an important nonlinear optical material for its ease of large-area growth for chip-scale integration, and we refer the reader elsewhere for details[95]. Integration with photonic platforms is still at early stages of research, so we point the reader towards comprehensive reviews of fundamental studies of 2D materials for nonlinear optics[96,97]. We focus here on guidelines for integrated photonic device design and the resulting nonlinear processes and applications, but the interested reader can find exhaustive data tables and best experimental practices for nonlinear optical materials in another review[98]. There, the reader can also find a detailed discussion of materials both on-chip and off-chip, including 0D to 3D materials suitable for nonlinear optics from terahertz to ultraviolet spectral ranges[98].

Nonlinear integrated photonics for frequency conversion

Broadband frequency conversion has produced coherent radiation at optical wavelengths spanning from the ultraviolet to the mid-infrared where there is a dearth of laser sources[99,100]. In addition, frequency conversion can enable all-optical switching and logic at telecom wavelengths[101] and high-resolution microscopy[102]. Seamless translation between disparate spectral ranges allows access to high-performance optical components such as lasers, cameras and detectors, which have only been perfected for a few spectral windows (visible and near-infrared). Despite the advantages offered by integrated optics design tools, new challenges accompany high-confinement waveguides, such as achieving good modal overlap between modes at distant wavelengths without compromising low loss and phase matching.

Nearly any parametric wave-mixing process involving two or more frequencies can be used for broadband classical frequency conversion, whereas QFC can only be achieved through very few processes such as Bragg scattering-FWM (BS-FWM), difference frequency generation (DFG) and sum-frequency generation (SFG). This distinction is due to more stringent requirements for QFC as it involves the conversion of quantum states of light without affecting their photon statistics. In the classical regime, second-harmonic generation (SHG), THG, SFG and DFG are the major processes for converting between widely separated spectral bands (say, visible to telecom) to expand the spectral range. FWM, by contrast, can be used for classical frequency conversion within a spectral band both between closely spaced frequencies and between widely separated spectral bands[103,104].

Expanding the spectral range: classical frequency conversion

Having a broad transparency window is a key requirement for frequency conversion to expand the spectral range of sources. LN, AlN and Si_3N_4, TiO_2 and GaP have been used to extend to shorter wavelengths owing to their large bandgap, which enables transparency windows in the visible region. Si, Ge and III–V materials such as GaAs and AlGaAs are more suitable for extending to longer wavelengths (towards the mid-infrared) owing to their smaller bandgaps.

Expanding to shorter wavelengths. SFG, SHG and THG can all be used for up-converting frequencies and generating short-wavelength light. Such short-wavelength sources find applications in ultraviolet–visible spectroscopy, high-resolution imaging, lithography, and for generating pump beams for quantum light sources. These processes are also important for self-referencing frequency combs through f–$2f$ and $2f$–$3f$ interferometry[105]. The generated power P_3 for SFG/SHG and THG (assuming undepleted pumps with input powers $P_j (j = 1,2)$ and no nonlinear loss) can be written as[106,107]:

$$P_3 \approx \frac{2\pi^2[\chi_{\mathrm{eff}}^{(2)}]^2 e^{-\alpha_3 L}}{\varepsilon_0 n_1 n_2 n_3 c \lambda_3^2} L_{\mathrm{eff}}^2 P_1 P_2 \mathrm{sinc}^2\left(\frac{\Delta \mathrm{kL}}{2}\right)\Gamma_{123};\ \mathrm{SFG}: \omega_3 = \omega_1 + \omega_2,\ \mathrm{SHG}: \omega_1 = \omega_2, \tag{2a}$$

$$P_3 \approx \frac{36\pi^2[\chi_{\mathrm{eff}}^{(3)}]^2 e^{-\alpha_3 L}}{\varepsilon_0^2 n_1^3 n_3 c^2 \lambda_1^2} L_{\mathrm{eff}}^2 P_1^3 \mathrm{sinc}^2\left(\frac{\Delta \mathrm{kL}}{2}\right)\Gamma_{1,3};\ \mathrm{THG}: \omega_3 = 3\omega_1, \tag{2b}$$

in which the indices 1 and 2 being identical for SHG. $\Gamma = \frac{\int(\prod_i E^*_{\mathrm{in},i})(\prod_j E_{\mathrm{out},j})\mathrm{d}A}{\prod_i(\int |E_i|^2 \mathrm{d}A)^{\frac{1}{2}}}$ is the mode overlap between fields at input frequencies $\omega_{\mathrm{in},i}$ and output frequencies $\omega_{\mathrm{out},j}$, and $L_{\mathrm{eff}} = 2(1 - e^{-(\alpha_1+\alpha_2-\alpha_3)L/2})/(\alpha_1 + \alpha_2 - \alpha_3)$ is the nonlinear interaction length beyond which loss counteracts upconversion. n_j is the index at frequency ω_j and wavelength λ_j with loss rate α_j (j = 1,2,3), and Δk is the phase mismatch (Box 2). The relative conversion efficiencies for SHG and THG are defined as $\eta_{\mathrm{SHG}} = P_3/P_1^2$ and $\eta_{\mathrm{THG}} = P_3/P_1^3$ in units of % W^{-1} and % W^{-2}, respectively,

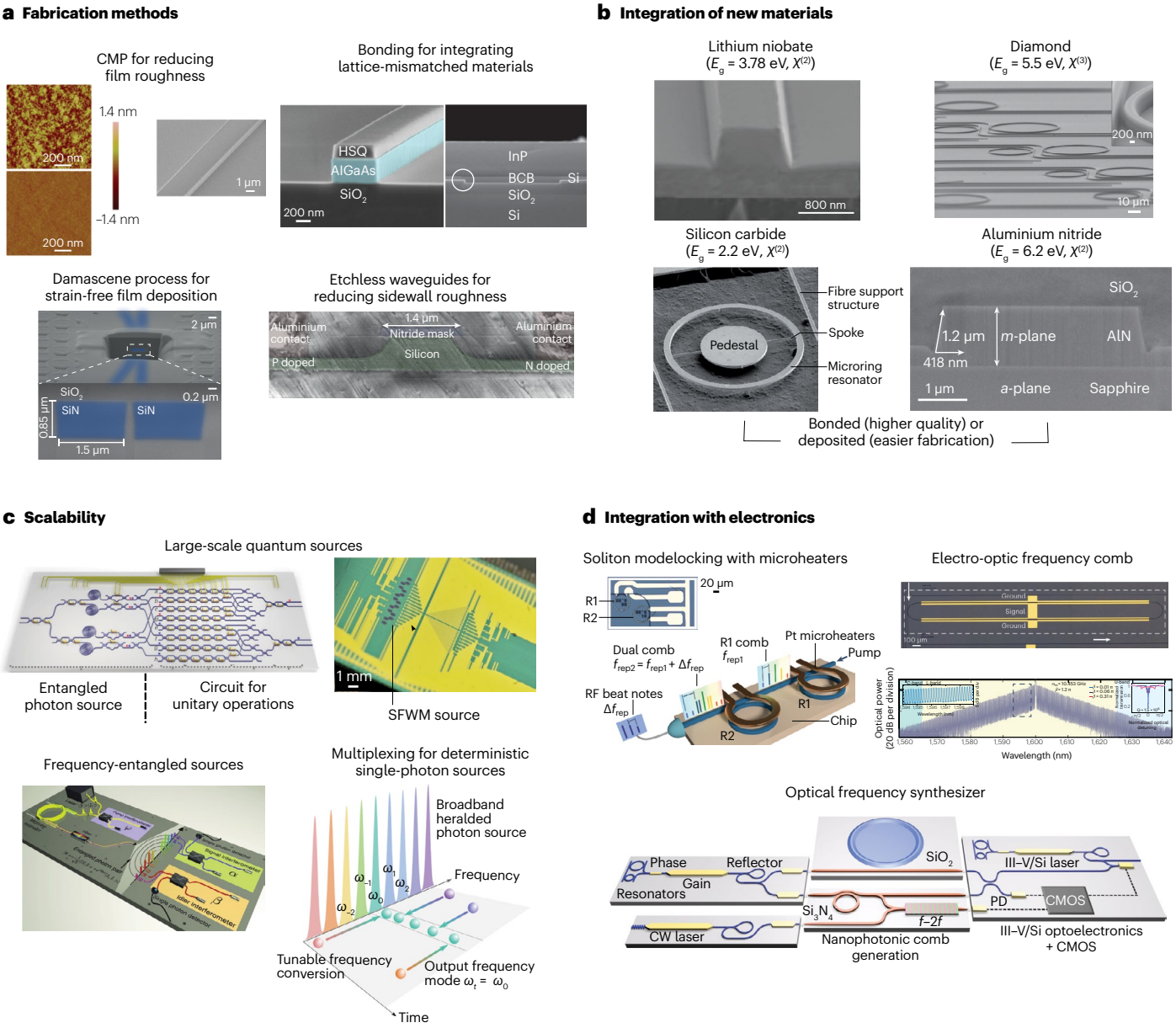

Fig. 2 | Integrated nonlinear photonics platform. a, Fabrication methods for enhancing nonlinear optical processes. **b**, New $\chi^{(2)}$ and wide bandgap materials that have been used to demonstrate nonlinear photonics. **c**, Large-scale demonstration of integrated nonlinear parametric sources for quantum information processing obtained by nanoscale lithography. **d**, Integrated electrodes have enabled applications such as soliton mode-locking using microheaters, electro-optic frequency combs and an optical frequency synthesizer. CMOS, complementary metal–oxide–semiconductor; CMP, chemical mechanical planarization; CW, continuous-wave; HSQ, hydrogen silsesquioxane; PD, photodetector; RF, radio frequency; SFWM, spontaneous four-wave mixing. Panel **a** reprinted with permission from ref. 13, Optica, with permission from ref. 31, Optica, from ref. 2, Springer Nature Limited, and with permission from ref. 54, Optica. Panel **b** reprinted from ref. 14, Springer Nature Limited, reprinted with permission from ref. 358, Optica, with permission from ref. 359, Optica, and with permission from ref. 360, Optica. Panel **c** reprinted from ref. 21, CC BY 4.0, with permission from ref. 23, AAAS, from ref. 287, Springer Nature Limited, and with permission from ref. 246, AAAS. Panel **d** reprinted from ref. 105, Springer Nature Limited, adapted with permission from ref. 176, AAAS, and reprinted from ref. 187, Springer Nature Limited.

owing to their power dependencies in the equations mentioned earlier.

The main requirements to boost η are low-loss ($\alpha_j L \ll 1$), strongly confining waveguides that satisfy phase matching Δk=0 and yet have a reasonable nonlinear spatial overlap Γ. For SHG and THG, a typical approach to achieve phase matching ($n_{\mathrm{eff1}} = n_{\mathrm{eff3}}$) is to match the index n_{eff1} of the fundamental mode at ω_1 with the index n_{eff3} of the higher-order transverse mode at ω_3. Such modal phase matching considerably decreases Γ owing to the different symmetries and spatial profiles at vastly different frequencies ω_1 and $\omega_3 = 2\omega_1$ or $\omega_3 = 3\omega_1$ (Figs. 3 and 4).

Engineering the mode overlap Γ_{123} in high-confinement waveguides through geometric considerations and composite material stacks has led to high conversion efficiencies of near-infrared light to ultraviolet wavelengths through SHG and THG, exceeding the performance of previous bulk demonstrations by four to five orders of magnitude and of low-confinement waveguides by one order of magnitude[106]. THG of green (532 nm) wavelengths was first demonstrated in ultrashort silicon nanowires using slow light[5,108]. With the introduction of $\chi^{(2)}$ materials such as GaAs, LN and AlN into integrated photonics, high-efficiency SHG is now possible. Additional improvements in film quality have considerably increased L_{eff}. These improvements in L_{eff} and mode overlap Γ_{123} have increased achievable conversion efficiencies (equation (2a)). The highest SHG conversion efficiency (250% W^{-1}) in a simple waveguide structure (that is, without any periodic poling or resonant enhancement) has been achieved in GaAs by leveraging its high $\chi^{(2)}$ and Γ_{123} enabled by small mode areas (0.5 $\mu\mathrm{m}^2$) and large overlap between the fundamental transverse electric (TE) and transverse magnetic (TM) modes at 2 µm and 1 µm, respectively[109]. To expand to shorter wavelengths, wide bandgap materials such as LN and AlN have allowed the generation of visible and ultraviolet light (306 nm), respectively, but mode overlap Γ_{123} still limits their efficiency[78,110,111] (equation (2a)). In this context, composite platforms (that is, waveguides consisting of layers of different materials) such as LN/TiO_2 (for SHG) and AlN/Si_3N_4 (for THG) have been used to provide a set of modes over which phase matching (Δk = 0, Box 2) and mode overlap Γ can be optimized[81,112] (Fig. 3d). For example, by using a vertical stacked structure composed of a $\chi^{(2)}$ (LN) and non-$\chi^{(2)}$ (TiO_2) waveguide, a pair of modes that typically would have zero overlap (Γ_{123} = 0) in a single-material waveguide owing to symmetry can have considerable overlap[112], producing a 773-nm light with η_{SHG}=36% W^{-1} (ref. 113).

Incorporating periodic poling and metasurface techniques with high-confinement waveguides allows for phase matching (Δk ~ 0) without using higher-order modes, overcoming the trade-off between phase matching (Δk) and mode overlap (Γ_{123})[107,114,115]. Nanofabricated microelectrodes have been used to apply a large electric field to precisely pole a thin film of LN with micron-scale precision for quasi-phase matching[107,114]. Up to 939% W^{-1} has been achieved for SHG of 780 nm light, an improvement of 40 times above low-confinement waveguides. Similarly, by leveraging nanophotonics, the conversion efficiency can be improved without the need for periodic poling. For example, an LN waveguide with an effective wavevector created by a 16-µm-thick phase-gradient metasurface, in which an array of dielectric antennas (a-Si) were patterned on top for SHG of 1,580–1,650 nm light, had impressive performance[115]; although the total conversion efficiency was low, the efficiency normalized to the metasurface thickness was commendable at ~1,660% $\mathrm{W}^{-1}\,\mathrm{cm}^{-2}$.

An effective $\chi^{(2)}$ that is obtained through strain, surface effects[116] or large electrical and optical fields allows centrosymmetric materials with a vanishing $\chi^{(2)}$ such as Si_3N_4, SiO_2 and Si to demonstrate second-order nonlinear phenomena. For instance, a $\chi^{(2)}_{\mathrm{eff}} = 3\chi^{(3)} E_{\mathrm{DC}}$ was realized in silicon using a strong DC field E_{DC} applied to the waveguides through spatially patterned p–i–n junctions[6]. Quasi-phase matching was implemented by alternating the applied DC field in successive periods of the patterned p–i–n, yielding η_{SHG} = 13% W^{-1} for conversion from 2.29 µm to 1.15 µm. Instead of DC fields, large optical fields can also induce an effective $\chi^{(2)}$ by producing a static DC field owing to charge migration[117,118]. These effects can produce a field-induced effective $\chi^{(2)}$ of approximately picometre per volt[119,120]. Note that both these kinds of field-induced effects are not permanent, and although the grating remains inscribed within the waveguide, the conversion efficiency decays over the course of days at room temperature[118].

Although the aforementioned discussion focused on single-pass waveguides, microresonators provide stronger nonlinear interactions owing to resonant enhancement at the expense of a narrower operation bandwidth limited to the resonator linewidth. The conversion efficiencies for resonant frequency upconversion can also be estimated from equation (2), except that the input powers are multiplied by their respective power enhancement factor F/π, in which F is the finesse of the resonator (Box 3). For example, high SHG conversion efficiencies have been reported in microresonators made of optically poled Si_3N_4 (47.6% W^{-1})[121], GaP (400% W^{-1})[122,123], polycrystalline AlN (2,500% W^{-1})[124], LN (10,000% W^{-1})[125] and AlGaAs (1,200% W^{-1})[126]. An even higher η_{SHG}= 17,000% W^{-1} was demonstrated by using single-crystal epitaxially grown AlN instead of polycrystalline AlN[124]. Note that resonant frequency converters often operate beyond the undepleted pump regime, and the aforementioned work shows pump depletion at a low input power of 3.5 mW with absolute conversion efficiency of η_{abs}=11%. In Si_3N_4 microresonators, frequency conversion from the telecom (1,550 nm) to visible (650 nm) using FWM was demonstrated with ~330 µW of power with 30% efficiency corresponding to 90,000% W^{-1} (ref. 104). The record for the largest conversion efficiencies reported on integrated platforms is η_{SHG}=5,000,000% W^{-1} (ref. 127), on the heels of earlier reports approaching 230,000% W^{-1} (ref. 44), both in PPLN microrings. This result was obtained despite moderate Q factors of 3.7×10^5, by engineering >90% modal overlap between interacting modes and achieving uniform periodic poling. Going by other metrics, the highest single-photon nonlinearity-to-loss ratios demonstrated in parametric nonlinear platforms are around 1% for PPLN microrings[127] and 1.5% for InGaP microrings[41].

Expanding to longer wavelengths. DFG and PDC are common methods to generate light sources at longer wavelengths, which allow the production of beams spanning far into the mid-infrared if the input frequencies are closely spaced. Additionally, FWM is widely used for expanding to longer wavelengths. Although sources of light in the mid-infrared, such as quantum cascade lasers, exist, room-temperature operation is still challenging owing to material limitations. Unlike the visible and near-infrared ranges, extensive work on extending silicon and germanium into the mid-infrared has been reported, as nonlinear losses (such as TPA) become negligible at $\lambda > 2.1$ µm for Si and $\lambda > 3.0$ µm for Ge[128]. DFG in PPLN on sapphire was used to generate 3.66-µm light with 200% W cm^{-2} by pushing the transparency window up to 4.5 µm (ref. 129). OPO[130], SHG and SFG were also used in tandem in nanophotonic LN to generate frequency-translated combs in the visible to mid-infrared region[131].

The first reports of frequency translation in silicon to the mid-infrared used pulsed pumps[132,133] and were followed by the use of CW pumps[103]. Optically poled Si_3N_4 waveguides have been used to generate

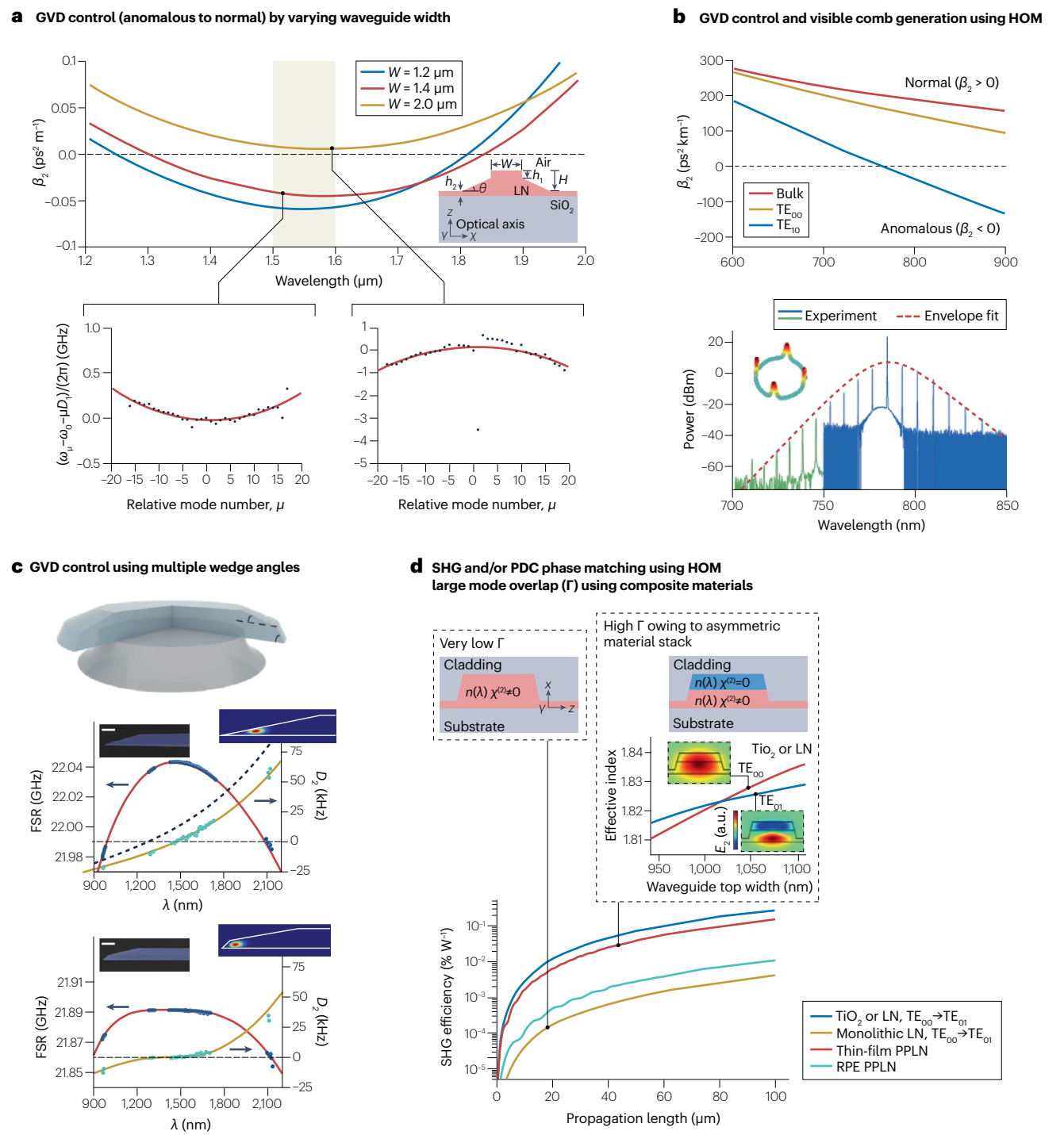

up to 1,890 nm light[134]. In the opposite direction, signals in the mid-infrared (2,440 nm) were converted to the telecom band (1,620 nm) with a parametric gain of 19 dB, to detect weak mid-infrared signals using efficient telecom detectors[135]. Beyond Si, III–Vs such as GaAs have shown conversion to longer wavelengths using DFG, either in suspended form or with an AlGaAs cladding, generating wavelengths up to 3,150 nm (ref. 136).

Quantum frequency conversion

For quantum communication and QIP, high performance devices with low loss and noise are essential to efficiently convert between disparate wavelengths while maintaining the quantum state (that is, photon correlations). A key application for broadband frequency conversion in chip-scale QIP systems is to interface high-performance components such as single-photon emitters, detectors and quantum memories

Fig. 3 | Basic dispersion engineering using waveguide geometry and/or higher-order modes. a, The group-velocity dispersion (GVD) can be engineered through the waveguide geometry, from normal to anomalous. **b**, At visible wavelengths, higher-order modes can provide anomalous GVD even when the fundamental mode is strongly normal owing to material dispersion and closeness to the bandgap. An example of visible soliton comb generation is depicted. **c**, GVD engineering by controlling the angle of multiple wedges in silica. Controlling the angle allows precise control over higher-order dispersion. **d**, Demonstration of high-efficiency second-harmonic generation (SHG) in a composite material stack of lithium niobate (LN, $\chi^{(2)} \neq 0$) and TiO_2 ($\chi^{(2)} = 0$). This asymmetric stack allows a large modal overlap (Γ) between TE_{00} and TE_{01} modes, which would otherwise have a very small overlap in monolithic LN. SHG efficiency is orders of magnitude higher in the composite stack compared with monolithic LN. FSR, free-spectral range; HOM, Hong–Ou–Mandel; PDC, parametric down conversion; PPLN, periodically poled lithium niobate; RPE, rapid proton exchange; TE, transverse electric. Panel **a** reprinted with permission from ref. 361, Optica. Panel **b** reprinted with permission from ref. 221, Optica. Panel **c** adapted from ref. 30, Springer Nature Limited. Panel **d** reprinted with permission from ref. 112, Wiley.

in the visible region with fibre communications infrastructure in the telecom band[137]. Future quantum networks could even require frequency conversion for interfacing photons at optical frequencies with remote superconducting quantum nodes operating at microwave frequencies[138]. Long-distance communication currently occurs over fibre optics; operation in the near-infrared region from 1,530 nm to 1,625 nm (C and L bands) has low fibre losses and allows for kilometres of propagation. However, single-photon emitters and quantum memories rely on atomic resonances that lie in the visible spectral range (such as diamond NV centre (637 nm), Rb (780 nm), Cs (852 nm), InAs quantum dot (980 nm))[139]. Similarly, Si avalanche photodiodes reach peak quantum efficiency in the range of 600–900 nm (ref. 140). QFC can also be used for smaller shifts in wavelengths for building multiplexed sources and active beam splitters in the frequency domain and for aligning quantum emitters that suffer from wavelength variation owing to inhomogeneous broadening.

Typically, QFC[141,142] involves the interaction of a weak (low mean photon number) quantum state at ω_0 with one or more strong classical beams at $\omega_{class1,2}$ in a nonlinear medium that generate a converted quantum field at the target frequency ω_t with identical quantum properties. Such an interaction can be achieved with both SFG[141] ($\omega_t = \omega_0 + \omega_{class}$) and BS-FWM[143] ($\omega_t = \omega_0 + \omega_{class1} - \omega_{class2}$). DFG[141] can also be used for QFC, when used in a non-parametric-amplifier configuration ($\omega_t = \omega_0 - \omega_{class}$), that is, when the strong classical beam is at one of the two lower frequencies. By contrast, DFG in a parametric-amplifier configuration ($\omega_t = \omega_{class} - \omega_0$)and FWM processes other than Bragg scattering such as modulation instability and phase conjugation[144] ($\omega_t = \omega_{class1} + \omega_{class2} - \omega_0$) result in parametric gain at ω_t, which amplifies vacuum fluctuations and produces spurious photons at ω_t that degrade the quantum state[143]. In practice, spurious photons can also be produced from other processes such as Raman scattering or cascaded SFG and spontaneous parametric down conversion (SPDC). Hence, the nonlinear processes that can produce quantum states of light (DFG/optical parametric amplification (OPA), PDC, modulation instability/phase conjugation-FWM, SHG, THG) are complementary to processes for QFC (SFG, BS-FWM and DFG/non-OPA).

BS-FWM offers a key advantage over $\chi^{(2)}$-based QFC for narrowband spectral translation[142]. The dispersion parameters $\beta_2, \beta_3 \ldots$ and the frequency separation between the pumps $\Delta\omega = \omega_{class1} - \omega_{class2}$ determine whether narrowband or wideband spectral translation occurs efficiently[143]. By contrast, narrowband QFC across less than ~50 nm based on DFG in $\chi^{(2)}$ media requires a strong pump in the mid-infrared or terahertz regime, which is challenging to both generate and guide. The phase mismatch for BS-FWM can be written as[21,142]:

$$\begin{aligned}\Delta k &= \beta(\omega_{p1}) - \beta(\omega_{p2}) + \beta(\omega_t) - \beta(\omega_0)\\ &\approx \frac{\beta^{(3)}}{6}[3\widetilde{\omega}\cdot\Delta\omega(\widetilde{\omega}+2\Delta\Omega)],\end{aligned} \tag{3}$$

in which $\Delta\Omega = \omega_{ZDW} - (\omega_{p1} + \omega_{p2})/2$ is the spectral separation of the zero-dispersion frequency ω_{ZDW} from the mean pump frequency such that $\beta_2(\omega_{ZDW}) = 0$, and $\Delta\Omega + \widetilde{\omega}$ is the spectral separation between ω_{ZDW} and the mean signal frequency $(\omega_0 + \omega_t)/2$ (Box 2). The equation mentioned earlier shows that BS-FWM is phase-matched when the pumps and signals are symmetrically placed around ω_{ZDW}, that is, when $\widetilde{\omega} = 0$. However, for wide spectral translations $\Delta\omega$ and fixed pump frequencies, the range of input signal frequencies that is phase-matched (that is, the acceptance bandwidth of the process) goes down, and higher-order dispersion terms affect the phase mismatch. Hence, it is desirable to have a QFC process with a wider acceptance bandwidth than the input quantum state. Although the process is phase-matched for both normal and anomalous GVD near the pumps as long as the symmetric spectral placement ($\widetilde{\omega} = 0$) is maintained, the pumps should preferably be in the normal-GVD range, to avoid parametric gain and added noise owing to spontaneous FWM.

Important foundational work has been demonstrated using low-confinement PPLN waveguides for frequency conversion based on SFG and DFG[137,141,145–160]. Several of these demonstrations interface among parametric single-photon sources, quantum dots[149,153,161], quantum memories[152] and single-photon detectors[162]. Similarly, PPKTP waveguides have shown QFC among widely spaced frequency bands such as the infrared and ultraviolet[151]. As the bandwidths of elements such as quantum memories are much narrower than those of single-photon sources, it is often beneficial to have bandwidth compression along with QFC[150]. Additionally, BS-FWM in fibres[142,163] has enabled QFC with near-unity conversion efficiencies of 95–99%, but using nonlinear fibres with lengths of tens to hundreds of metres[21,164]. In PPLN microring resonators, efficient SFG with external quantum efficiency of 65% with only 104 μW has been shown. The conversion probability of a single pump photon was measured to be 10^{-5} with a coupling strength of 9.1 MHz (ref. 165).

High-confinement nanophotonic resonators have markedly reduced the requirements on pump powers and interaction lengths for BS-FWM-based QFC compared with their fibre-based counterparts. BS-FWM works well to convert photons between vastly different spectral ranges because it avoids the noise from the pump, but it has been used within narrow spectral ranges as well, which is pivotal for frequency-domain QIP. For instance, BS-FWM in compact Si_3N_4 microrings with 40 μm radius has shown both frequency upconversion and down-conversion between 980 nm and 1,550 nm, with >60% single-photon efficiency, using reasonable pump powers ~60 mW (ref. 139). On the same platform, a narrowband spectral translation around 980 nm was associated with a lower efficiency of 25%. Similar BS-FWM strategies have also translated classical soliton microcombs consisting of multiple frequency modes, thus broadening the bandwidth of the comb by 60% (ref. 166). Silicon waveguides have been used for single-photon-level frequency translation with broad acceptance bandwidths, but

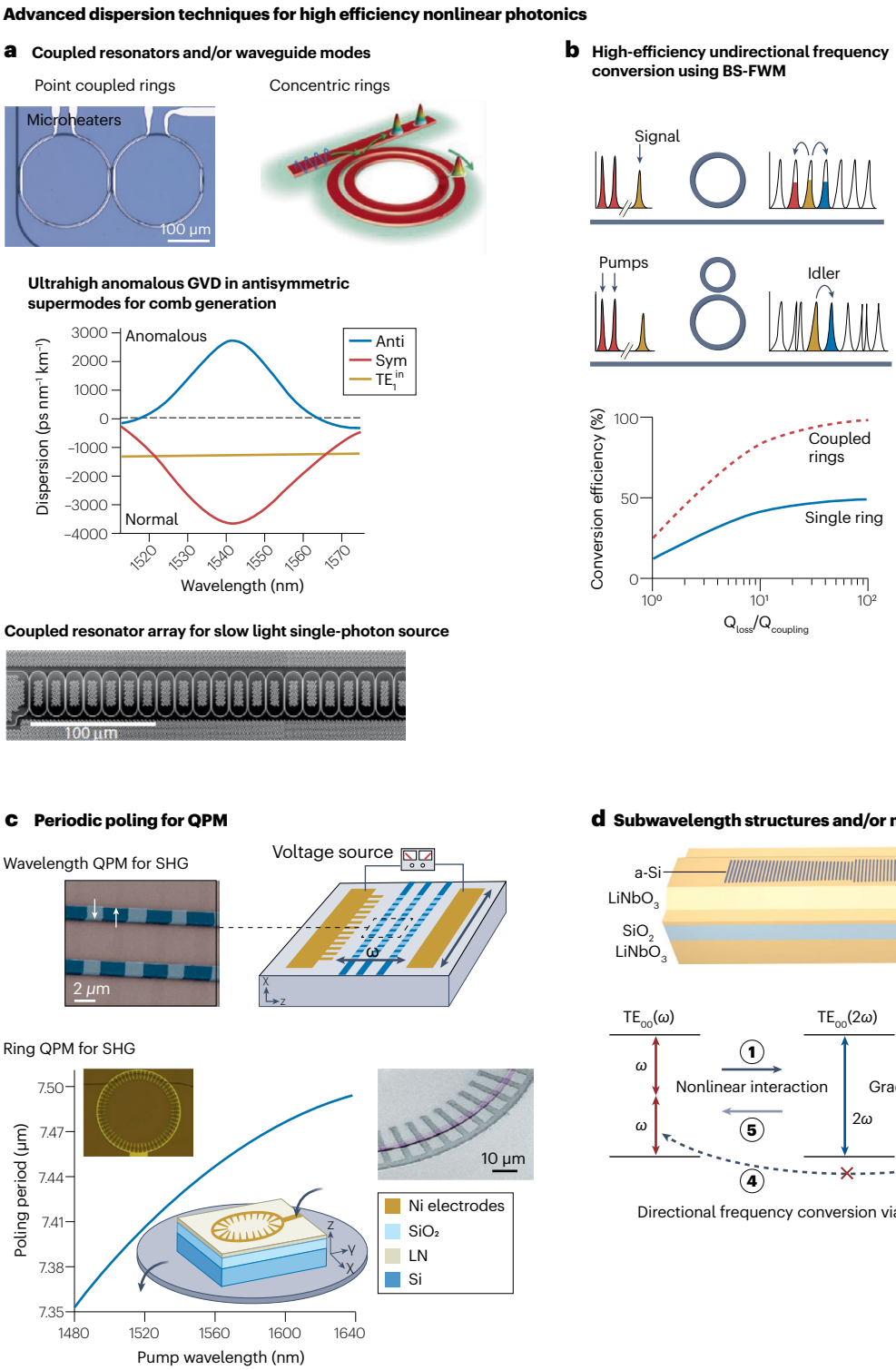

with conversions efficiencies limited to 15% owing to nonlinear losses induced by the pumps[3,57]. Si_3N_4 (ref. 167) and AlN ($\chi^{(2)}$)[80] microrings have also attained the 'strong coupling' regime, albeit with classical light, whereby the rate of coherent conversion between photons at different frequencies is higher than the photon decay rate in the ring.

Extending this coherent conversion to quantum states of light would be promising for QIP. In this regard, true single photons emitted by a quantum dot have been frequency-translated by 12.8 nm to a target wavelength of 917 nm with a 12.8% conversion efficiency, limited by the emitter linewidth[161].

Fig. 4 | Advanced dispersion engineering techniques for high-efficiency nonlinear photonics. a, Coupled rings allow for extremely high anomalous group-velocity dispersion (GVD) owing to the strong dispersion near the avoided crossing. They can be used for microcomb generation at arbitrary wavelengths. Coupled-resonator optical waveguide for heralded single-photon source in Si utilizing slow-light-based GVD engineering. **b**, Coupling non-identical rings allows suppression of spurious idlers by creating unequally spaced resonance frequencies, enabling high-efficiency unidirectional quantum frequency conversion to the desired target mode based on Bragg scattering four-wave mixing (BS-FWM). **c**, Periodic poling of high-confinement $LiNbO_3$ (LN) rings and waveguides for ultra-high efficiency second-harmonic generation (SHG). **d**, Phase-matching-free SHG using gradient metasurfaces with subwavelength structuring. The solid arrows denote allowed conversions. The dashed crossed arrows represent phase-mismatched or low-efficiency conversions. QPM, quasi-phase matching; TE, transverse electric; TM, transverse magnetic. Panel **a** reprinted with permission from ref. 362, Optica, and with permission from ref. 363, Wiley. Panel **b** reprinted with permission from ref. 282, AIP, and from ref. 169, CC BY 3.0. Panel **c** reprinted with permission from ref. 107, Optica, and with permission from ref. 364, Optica. Panel **d** reprinted from ref. 115, Springer Nature Limited.

Current challenges in QFC using BS-FWM in microrings include the generation of undesired idler fields at frequencies other than the target and a maximum conversion efficiency that is limited by the strength of overcoupling (Q_C/Q_L)[168]. Because all the ring modes are equally separated by the same spacing as the pump frequency separation $\Delta\omega$, conversion to undesired idler modes adjacent to the target mode is usually observed[139], as both output frequencies $\omega_{t\pm} = \omega_{in} \pm \Delta\omega$ are phase-matched to the lowest order. To mitigate this undesired conversion and achieve truly unidirectional frequency conversion, future work could use coupled rings with different radii, which result in unequally spaced resonance frequencies[138,169]. Classical experiments in this regime have been promising. To mitigate the issue of a limited conversion efficiency, one could either build highly overcoupled rings or avoid rings altogether and use long spiral waveguides[170]. The use of long waveguides could also minimize the generation of undesired idlers as the phase mismatch for these modes accumulates over the long length[171]. In a radically different approach, adiabatic frequency conversion has been proposed for ultrabroadband spectral translation without compromising the conversion efficiency, using longitudinally varying silicon waveguides[172]. Finally, it is important to go beyond demonstrations of spectral translation and use on-chip platforms for applications such as quantum imaging[173], multiplexed deterministic single-photon sources[21], infrared spectroscopy[99] with visible light[174] and interfacing microwaves with optical frequencies.

Nonlinear photonics for classical and quantum sources and information processing

Frequency-comb generation

Since the late 2000s, microresonator-based frequency combs (microcombs) have been generated in a plethora of material platforms. The set of coherent, equidistant spectral lines produced have applications in optical clocks, metrology, ultrafast LiDAR[27,28,175], spectroscopy[29,176,177], communications[178–180], optical coherence tomography imaging[181,182], astronomical spectrograph calibration[183,184] and direct optical frequency synthesis[105]. Starting with their initial demonstration in SiO_2 microtoroids in 2007 (ref. 185), frequency combs (Box 1, equation (6)) have been miniaturized to the chip scale using FWM in nonlinear microresonators. Si_3N_4, in particular, has been highly successful for microcomb generation owing to its low loss, important nonlinearity, on-chip integrability and dispersion engineering capability[186], the obtained platforms spanning wide wavelength ranges (~0.5–3.5 µm) (Figs. 1 and 5). Although the majority of microcombs use the Kerr nonlinearity, chip-scale electro-optic (EO) frequency combs using LN and Si resonators have gained ground over the past years[187–189].

The key figures of merit for microcomb platforms are typically a low parametric oscillation threshold, wide bandwidth and high pump-to-comb conversion efficiency, which are difficult to achieve simultaneously. The pump threshold, P_{th}, depends primarily on Q_L^2/V (Box 1, equation (7)) being minimum in the slightly undercoupled regime, whereby Q_L and V are the loaded quality factor and the mode volume, respectively. Additionally, P_{th} reduces linearly with n_2 but quadratically with Q_L. Hence, the low n_2 of materials such as crystalline fluorides and silica can be compensated by their record high Qs, which resulted in ultra-low threshold powers of 50 µW to approximately milliwatts in their very first demonstrations[185,190]. Improved fabrication techniques have enabled the lowering of threshold powers to similar levels in planar chip-integrated platforms with higher n_2 (Si_3N_4 (ref. 31) and AlGaAs[13,38]). At higher powers ($P_{in} \gg P_{th}$), a large number of frequency modes start oscillating, and nontrivial nonlinear interactions between these modes produce filled-in combs in either noisy states or temporal soliton states for $P_{in} > \sim 10P_{th}$.

This remarkable feature of microcombs — the generation of hundreds to thousands of frequencies from a single frequency input — overturned pre-existing ideas from fibre soliton combs that required pulsed multifrequency inputs. Soliton mode-locked microcomb states are characterized by low noise and coherent pulses, and hence their deterministic generation in microresonators[191] was pivotal to applications in frequency metrology, spectroscopy and optical distance measurement. Soliton mode-locking involves competing nontrivial, nonlinear and thermal dynamics, for which we refer the reader to excellent reviews[9]. Here, we note that soliton mode-locking has been achieved by fast tuning of either the pump wavelength (MgF_2, SiO_2 and AlN)[191–193] or pump power (Si_3N_4)[194], by integrated thermal tuning of the resonator (Si_3N_4)[195] or by megahertz-rate piezoelectric tuning using AlN on Si_3N_4 (ref. 196). Specifically, microheater-based tuning and piezoelectric tuning enable scalable on-chip incorporation of the control technique[195] and allow tuning of multiple microcomb generators on the same chip pumped[176] — a feat that is challenging using pump tuning. On the contrary, fast tuning is not necessary for soliton generation in LN Kerr microresonators[197] owing to the photorefractive effect of the material, which causes an intensity-dependent decrease of refractive index, as opposed to the positive thermo-optic effect in the platforms mentioned earlier. Similarly, soliton crystal states[198] can be generated without fast tuning mechanisms and often offer robust and stable operation as opposed to single-soliton states[199].

Microcombs have also been generated in Hydex[37], diamond[14], GaP[200], SiC[68,69], AlN and AlGaAs-on-insulator[13]. The past few years have witnessed soliton mode-locking (SiC[25], AlGaAs[201] and AlN[43,202]) or octave spanning operation (SiC[16] and AlN[43,202]) in several of these platforms. AlN, AlGaAs and LN are particularly appealing owing to their non-zero $\chi^{(2)}$, which enables both EO tuning/switching of comb lines[203,204], as

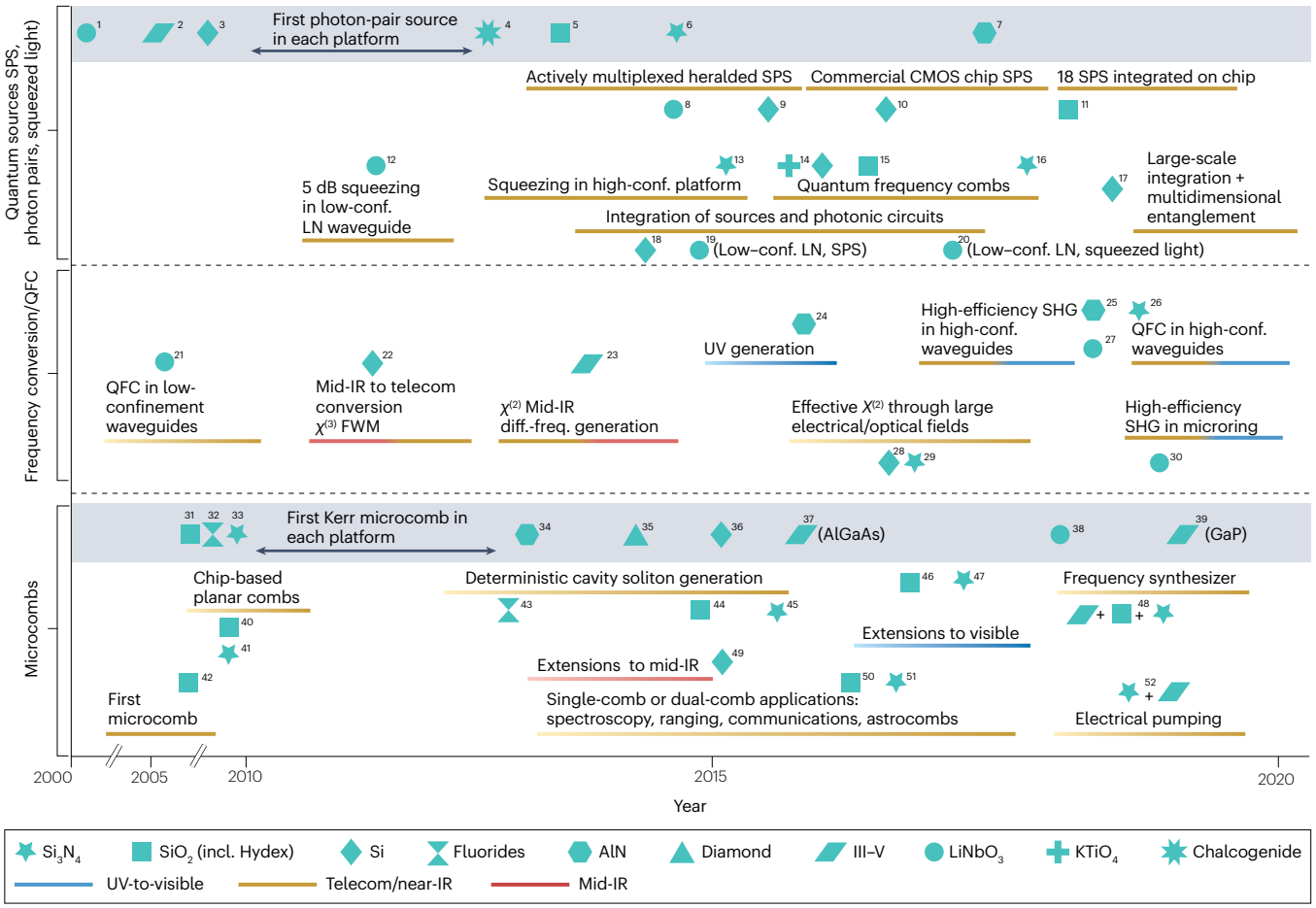

Fig. 5 | Notable first demonstrations and milestones in chip-scale integrated platforms. Quantum sources[23,248,249,257,260,262,264,270–272,274,275,284,287,300,315,322,331,365,366] (top), frequency conversion and quantum frequency conversion (QFC; middle row)[6,78,103,107,117,124,136,151,161,162,364] and microresonator Kerr frequency combs (bottom row)[2,13,14,26–29,36,37,42,105,175–185,191,192,195,200,204,206,222,223,367]. Each material is represented by a unique shape. The shading of the boxes is qualitatively red for mid-infrared (IR), yellow for telecom/near-IR and blue for ultraviolet (UV)-to-visible. Note that the *x*-axis representing time is compressed before 2010 to highlight recent developments over the past decade. CMOS, complementary metal–oxide–semiconductor; FWM, four-wave mixing; LN, $LiNbO_3$; SHG, second-harmonic generation; SPS, single-photon source. References for each data point: 1, ref. 260; 2, ref. 262; 3, ref. 270; 4, ref. 365; 5, ref. 272; 6, ref. 275; 7, ref. 257; 8, ref. 366; 9, ref. 300; 10, ref. 271; 11, ref. 248; 12, ref. 322; 13, ref. 249; 14, ref. 331; 15, ref. 23; 16, ref. 274; 17, ref. 287; 18, ref. 284; 19, ref. 264; 20, ref. 315; 21, ref. 162; 22, ref. 103; 23, ref. 136; 24, ref. 78; 25, ref. 124; 26, ref. 161; 27, ref. 107; 28, ref. 6; 29, ref. 117; 30, ref. 364; 31, ref. 185; 32, ref. 367; 33, ref. 36; 34, ref. 42; 35, ref. 14; 36, ref. 2; 37, ref. 13; 38, ref. 200; 39, ref. 200; 40, ref. 37; 41, ref. 36; 42, ref. 185; 43, ref. 191; 44, ref. 192; 45, ref. 195; 46, ref. 222; 47, ref. 223; 48, ref. 105; 49, ref. 2; 50, refs. 27–29; 51, refs. 175–184; 52, refs. 26,206.

well as EO comb generation on the same platform[187]. AlGaAs also holds promise for the monolithic integration of the pump laser with the microcomb generator. In this direction, important progress has been made by interfacing an Si_3N_4 chip with a III–V gain chip, enabling electrical pumping[26,205,206] and even battery-powered[26] or turnkey soliton[207] operation.

The bandwidth of microcombs is strongly controlled by dispersion, and the broadest soliton combs have been achieved in 1-THz-FSR Si_3N_4 rings[194,208]. The maximum 3-dB bandwidth of a soliton frequency comb is approximately[191]

$$\Delta f_{3\mathrm{dB}} = 0.224\sqrt{\frac{Q_\mathrm{L}^2}{Q_\mathrm{c}}}\sqrt{\frac{P_\mathrm{in}\cdot \mathrm{FSR}\cdot n_2}{-\beta_2 c A_\mathrm{eff}}} = 0.224\sqrt{\frac{Q_\mathrm{L}}{Q_\mathrm{c}}}\sqrt{\frac{\gamma F P_\mathrm{in}}{-\beta_2}}, \qquad (4)$$

which shows that a small but anomalous dispersion ($\beta_2 < 0$) produces the broadest combs, provided the nonlinear factor $\gamma = 2\pi n_2/\lambda_p A_\mathrm{eff}$ is enhanced by strong waveguide confinement (small A_eff) and a large material n_2. The bandwidth is maximized for compact resonators with a large FSR and at critical coupling $Q_\mathrm{c} = 2Q_\mathrm{L}$ for fixed intrinsic losses per unit length (fixed Q_i). This expression works well for silica and crystalline fluoride combs, which have moderate bandwidths (<100 nm), but overestimates the bandwidth for large-FSR Si_3N_4 and silica combs, which can span an octave[209]. For such ultrabroadband microcombs, higher-order dispersion terms (β_3,...) could make the dispersion normal far away from the pump, limiting the comb bandwidth to ~3 $|\beta_2|/\pi\beta_3$ (ref. 209). To achieve higher-order dispersion engineering, extremely precise control over waveguide dimensions and material composition is essential (Fig. 3a–c). Besides the conventional techniques of

dispersion engineering using waveguide cross-sections[210] (for microrings) and resonator shapes (for microtoroids and wedge resonators[30]), several efforts have focused on using thin films of a completely different material, for example, hafnia[211] or electrically gate-tunable graphene[212]. Although most work has focused on anomalous-dispersion microcombs, normal-GVD microcombs, even though narrower in bandwidth, are attractive for non-traditional wavelengths and for applications such as coherent communications in which power efficiency is more important than comb bandwidth with 30–40% pump-to-comb power conversion efficiencies being reported[213–220].

New applications such as optical coherence tomography[181,182] and access to alkali atomic lines have garnered interest in frequency-comb generation beyond the near-infrared into the visible spectral range[221–224]. At the other end of the spectrum, microcombs in Si_3N_4 (ref. 225), Si (ref. 2) and LN[226] are being driven into the mid-infrared 'molecular fingerprint' region owing to the strong rotational–vibrational absorption lines of many molecules. Si rings have proven very successful in this region, owing to the absence of TPA beyond 2.2 µm and the ability to extract carriers generated from three-photon absorption using p–i–n diodes[2]. In fact, TPA and free-carrier-induced losses inhibit Si parametric oscillation near 1,550 nm (ref. 227), despite theory predictions to the contrary[228]. Moreover, extending microcombs further into the mid-infrared has inspired the exploration of Ge microresonators, with potential for low loss and high nonlinearity[62].

The compact size of microresonators results in a large FSR, making them particularly suitable for high-f_{rep} applications such as coherent communications (f_{rep} > 100 GHz)[178,229], high-power coherent terahertz generation (f_{rep} > 100 GHz)[230] and astronomical spectrograph calibration (f_{rep} ~10–30 GHz)[183,184]. Although the use of individual comb lines for wavelength-division multiplexed communications was proposed in initial reports of chip-scale combs[36,37], the first demonstration of the use of Kerr combs as a wavelength-division multiplexed source was presented in 2012, where an open eye and error-free operation was demonstrated under conditions of mode-locked operation[231]. In 2017, 179 lines of two interleaved combs was demonstrated as optical carriers for transmitting massively parallel, extremely high-bit-rate data streams (>50 terabit s^{-1})[178]. Single-soliton mode-locked states with predictable and stable spectral envelopes avoiding mode crossings and with reasonably broad bandwidths were helpful for this demonstration. Ultrabroadband spectral translation has uncovered new wavelength bands around 2 µm (ref. 229) beyond the telecom band for frequency-comb-based coherent communications or to extend the spectral reach of microcombs to 1.6 octaves[166]. Beyond single-soliton states, soliton crystals[199] and dark-pulse solitons[232] have also enabled ultrafast and ultradense coherent communications, increasing data rates up to 1.84 petabits s^{-1}. Other applications such as optical ranging (LiDAR)[27,28], spectroscopy and frequency metrology require lower f_{rep}, and the latter benefits from ultrabroad bandwidths spanning an octave, so that the combs can be self-referenced by an f–$2f$ interferometer. Several of these applications (Fig. 5) including spectroscopy[29,176,177], ranging[27,28] and communications[178] use dual combs to markedly speed up data acquisition by orders of magnitude and compress both amplitude and phase information spanning the optical comb bandwidth (approximately tens of terahertz) to electronically accessible microwave bandwidths (megahertz to gigahertz)[9,29,176,177]. A dual comb consists of two combs that are mutually coherent but with slightly different f_{rep}. This enables straightforward acquisition of spectral information at high speeds by obviating mechanically moving parts of bulky spectrometers.

Leveraging the benefits of multiple nonlinear platforms resulted in an impressive demonstration of an optical-frequency synthesizer — an instrument for on-demand generation of a precise, stable optical frequency signal referenced to a microwave clock[105], by specifying the two RF frequencies f_{rep} and f_{ceo} and the integer m in equation (4). Here, a silica microresonator generating a narrowband but low f_{rep} comb (f_{rep} = 22 GHz, accessible with microwave electronics) was combined in a gearbox-like fashion with an Si_3N_4 microring generating a 1-THz-f_{rep} but ultrabroadband octave-spanning comb (required for f–$2f$ self-referencing) (Fig. 3d). A large octave-spanning bandwidth Δf_{3dB} typically necessitates a large microwave-inaccessible f_{rep} > 200 GHz within reasonable pump powers (equation (4)), which explains why multiple separate chip platforms were used.

The generation of robust, fully integrated microcombs compatible with silicon photonics is yet to be demonstrated; however, developments[26,105,206] have been promising towards the complete integration of the laser, microcomb generator, SHG and f–$2f$ self-referencing on a single chip, as all these components have been realized individually. Another avenue would be the integration of microfluidics with microcombs for lab-on-a-chip sensing and spectroscopy[233]. Finally, novel material approaches such as plasmonic enhancement, organic functionalization and $\chi^{(2)}$ processes/quadratic solitons could lead to lower power operation and relaxed phase-matching constraints[234–239].

Quantum light sources

Integrated quantum photonic systems are currently limited by the ability to integrate many identical quantum light sources on a chip — a thousand or more may be required for QIP applications[240,241]. Cluster-state quantum computing, arguably the most promising protocol for photonic computing, relies on measurements of a large multipartite entangled quantum state (that is, the cluster state) based on several quantum light sources[242–244]. This protocol eliminates the need for two-qubit gates, which have been challenging to implement owing to weak single-photon nonlinearities. Eventually, fault-tolerant quantum computation demands integrating and manipulating many quantum sources, whereby each error-corrected logical qubit is obtained from multiple physical qubits[245]. Spectral, spatial and temporal modes of a photon further allow for generating entanglement spanning high-dimensional Hilbert spaces. Such entanglement is a useful resource for quantum sensing and communication applications such as quantum teleportation, entanglement swapping, quantum repeaters and entanglement-based quantum key distribution.

Quantum sources based on nonlinear nanophotonics are attractive owing to their monolithic, scalable integration with photonic circuits to manipulate quantum states on the same chip. Integrated photonic platforms based on $\chi^{(2)}$ and $\chi^{(3)}$ materials have been used to generate quantum light in two regimes[240]: the discrete variable, or qubit, regime using single-photon and few-photon sources[246–248] and the continuous variable regime using squeezed light[249–251]. These sources can be lithographically defined in the same platforms that are used for quantum photonic circuits such as silicon[246], silicon nitride[252,253] and Hydex[24]. Moreover, multiple parametric quantum sources can be interfered with high visibility to generate entanglement at room temperature owing to their identical nature (as opposed to solid-state emitters)[254,255], confinement in a well-defined spatial mode and the phase stability of integrated photonics.

Discrete variable — SPS. In nonlinear nanophotonics, SPDC and spontaneous four-wave mixing (SFWM) are most commonly used to

produce single photons with high indistinguishability and spatial and/or spectral mode purity[247]. Both SPDC and SFWM generate pairs of photons in signal and idler modes when operated at low pump powers, and these modes can be distinguished based on polarization, frequency or other degrees of freedom, determined by waveguide dispersion. The source brightness or signal and idler (s/i) pair production rate, ρ, for a photonic cavity pumped by an input of power P_p at a frequency ω_p depend on the Q's and the mode volume V as[256,257]:

$$\rho \approx \begin{cases} \dfrac{9\left[\chi_{\mathrm{eff}}^{(3)}\right]^2}{16\varepsilon_0^2\omega_{\mathrm{p}}(n_{\mathrm{p}}^2 n_{\mathrm{s}} n_{\mathrm{i}})^2}\left(\dfrac{Q_{\mathrm{p}}^3}{V^2}\right)P_{\mathrm{p}}^2 = (\gamma P_{\mathrm{p}} L)^2\left(\dfrac{F}{\pi}\right)^3\dfrac{FSR}{2}\,; \text{SFWM} \\ \dfrac{8\left[\chi_{\mathrm{eff}}^{(2)}\right]^2}{\varepsilon_0(n_{\mathrm{p}} n_{\mathrm{s}} n_{\mathrm{i}})^2}\left(\dfrac{Q_{\mathrm{p}} Q_{\mathrm{s}} Q_{\mathrm{i}}}{V}\right)P_{\mathrm{p}}\,; \text{SPDC} \end{cases} \quad (5)$$

in which $V = 2\pi R A_{\mathrm{eff}}$ (see Box 3 for A_{eff} which accounts for pump–signal–idler mode overlap), $\chi_{\mathrm{eff}}^{(2)}$ and $\chi_{\mathrm{eff}}^{(3)}$ are the effective second-order and third-order nonlinear susceptibilities, $n_{p,s,i}$ is the pump, signal and idler indices, $Q_{p,s,i}$ is the quality factor at the pump, signal and idler frequencies, F is the cavity finesse, FSR is the cavity-free spectral range, γ is the nonlinear parameter and L is the cavity length. The pair generation rate, ρ, can be increased considerably using high finesse cavities.

The first class of SPS based on SPDC is in their early stage of development owing to the new integration of $\chi^{(2)}$ platforms such as AlN, LN and optically poled Si_3N_4 on chip. Low-confinement integrated platforms such as LN[258–260] and KTP waveguides, modally phase-matched LN cavities[261] and III–V materials based on GaAs/AlGaAs[74,262,263] can generate photon pairs as well as heralded SPS, albeit with millimetre-to-centimetre-scale lengths. Developments in periodically poled waveguides have shown reconfigurable photonic circuits that are monolithically integrated with entangled photon sources[264]. In high-confinement platforms, the first nanophotonic SPDC SPS was realized in AlN microrings, utilizing modal phase matching between a TM_2 pump mode at 775 nm and the TM_0 signal and idler modes at 1,550 nm (ref. 257). The strong spectral and spatial confinement and the integration of waveguide-coupled superconducting NbTiN detectors led to a high generation rate of 20 MHz mW^{-1}, comparable to state-of-the-art LN waveguide sources, with a heralded second-order autocorrelation of $g^{(2)}(0) = 0.09$ signifying single-photon purity. The second-order autocorrelation is defined as $g^{(2)}(\tau) = \frac{\langle n_1(t) n_2(t+\tau)\rangle}{\langle n_1(t)\rangle\langle n_2(t+\tau)\rangle}$, in which $n_{1,2}(t)$ is the number of counts on the respective detector at time t, and τ is the time delay. An SPDC source of correlated photon pairs has also been reported in nanophotonic high-confinement LN[265,266]. Similarly, a PPLN microresonator was used to generate heralded single photons at ~2.5 MHz μW^{-1} rate with $g^{(2)}(0) = 0.008$. The effective $\chi^{(2)}$ nonlinearity in all-optically poled silicon nitride has also been used to generate SPDC photons with two-photon interference visibilities of ~99% and to demonstrate entanglement[267].

The second class of SPS based on SFWM relies on the more ubiquitous $\chi^{(3)}$ materials in CMOS-compatible silicon photonics[268–270]. Multiphoton absorption and its associated free-carrier effects are less problematic for photon pair production in Si than for comb generation and squeezed light generation because low pump powers are sufficient. The effect of free carriers can be mitigated by extracting them using reverse-biased p–i–n structures, which can double the generation rate without compromising the high coincidental-to-accidental ratio or CAR (>600) of Si microring sources[49]. The CAR quantifies the ratio of useful photon pairs emitted, to spurious photons produced by noise and multiphoton emission events or sacrificed to losses. As another impressive development, correlated photon pairs were generated in a standard commercial 45-nm CMOS foundry[271].

Since the mid-2010s, a few groups have investigated sources in larger bandgap $\chi^{(3)}$ platforms such as silica[248,272,273], Si_3N_4 (refs. 274–277) and chalcogenides[278] for their lower linear and multiphoton losses, which enable more complex photonic circuits, albeit at a larger footprint than the higher-index Si platform. Particularly in Si_3N_4, this approach has enabled the obtention of a single-photon pair source, which is tunable in the visible range whereas the idler photon is in the telecom band[277]. The ultra-high Q resonators in these low-loss platforms produce photon pairs in discrete narrow spectral modes, making them useful for interfacing with quantum memories which have bandwidths in the megahertz to gigahertz range[279]. Non-resonant waveguide sources, however, produce broadband photon pairs whose bandwidth is determined by phase matching. Such broadband photons are useful for frequency multiplexing and for quantum imaging, hyperspectral imaging and spectroscopy with undetected photons[280].

In contrast to SPDC sources, pump suppression is substantially more challenging for SFWM single-photon sources as the pump is spectrally close to the much weaker generated photons, resulting in the degradation of CAR and $g^{(2)}(0)$. Although ρ increases linearly and quadratically with P_p for SPDC and SFWM sources, the CAR and the $g^{(2)}$ degrade with increasing pump power owing to increasing multiphoton emission. High performance requires strong suppression of the bright pump because it is orders of magnitude higher in power than the generated signal and idler photons. In this regard, SFWM-correlated photons were generated in an Si microring, followed by the demonstration of high-extinction pump suppression of 95 dB using a Bragg reflector and thermo-optically tuned add-drop microrings[281], without the need for off-chip filtering, resulting in a CAR of 50. Using off-chip filtering of an Si microdisk photon-pair source, a high CAR of 1,300 has been reported along with an extremely high spectral brightness. Beyond single silicon rings, coupled microrings in the form of coupled resonator optical waveguides (CROWs) have also demonstrated dispersion-engineered single-photon sources[282,283] using the concept of slow light.

Large-scale demonstrations of integrated quantum photonic circuits have shown high-visibility interference between multiple SPS within waveguides[246,264,284] and rings[285,286] combined with complex qubit operations for multidimensional quantum entanglement[246]. In silica, the integration of 18 single-photon sources on the same chip was demonstrated and five heralded single-photon sources were used to show three-photon quantum interference[248]. For fully integrated quantum photonics, it is important to integrate several single-photon and/or photon-number-resolving (PNR) detectors with a large number of quantum sources as well as photonic circuits, and initial steps in this context have already been reported[257]. The use of silicon photonics has resulted in impressive progress towards[246] realizing multidimensional quantum entanglement, arbitrary two-qubit operations[287] and even qudit (d-level system) operations, by integrating up to 16 silicon SFWM sources, reconfigurable beam splitters and waveguide crossings on a single chip. However, these demonstrations have been limited to bipartite (two-photon) multidimensional entanglement. Scaling up to a much larger number of photons, in addition to increasing dimensionality, is of paramount importance for future applications in QIP and quantum-enhanced sensing.

An alternative to path-encoding-based multidimensional entanglement is to generate correlated photons using an intrinsic photonic degree of freedom such as frequency, time or transverse spatial modes. For example, spectral modes allow for the generation of quantum frequency combs, in which biphotons are emitted into symmetrically placed signal and idler modes, using the same microrings as used for classical microcombs, but at pump powers well below threshold. Such quantum combs[288] have demonstrated time-bin entanglement and high-dimensional frequency-bin entanglement in a single spatial mode, using Hydex microrings[23,24,288,289], Si_3N_4 microrings[274], PPKTP waveguides[290], LN microrings[291] and silicon microdisks[292]. The advent of classical soliton microcombs in SiC has also led to studies of second-order photon correlations[25] on the same platform, enabled by a high dynamic range (~180 dB) single-photon spectrometer to overcome the aforementioned pump suppression issues concomitant to FWM SPS. Frequency-domain quantum (Hong–Ou–Mandel) interference of correlated pairs has been demonstrated using SFWM in an Si_3N_4 microring and BS-FWM in fibre for frequency-domain mixing[293]. To fully harness quantum frequency combs for applications, a larger number of photons would need to be entangled, as shown off-chip for six photons using path, polarization and orbital angular momentum degrees of freedom[294]. Besides spectral modes, transverse spatial modes in high-index-contrast multimode waveguides offer a path for generating and manipulating entanglement and quantum interference[252,295].

The probabilistic nature of parametric SPS is a major challenge to its widespread adoption in quantum technologies, in contrast to solid-state emitters which produce photons deterministically but with lower indistinguishability[254,255]. Moreover, the rate of multiphoton emission increases when such SPS is pumped at higher powers, fundamentally limiting the heralding efficiency of heralded SPS to 25% (ref. 296). A way to overcome this and achieve deterministic operation is to actively switch photons from several identical heralded SPS[297], which increases the photon generation rate without increasing multiphoton events. Such switching has been proposed or demonstrated using various degrees of freedom of a photon: temporal multiplexing[298], spatial multiplexing[299] or spectral multiplexing[21]. Silicon nanowire SFWM sources were also used for time multiplexing[300]. Spectrally multiplexed heralded SPS, currently realized in fibres[21], could be integrated using different platforms. Major challenges in integrating multiplexed SPS include the requirement for long low-loss delays to buffer the heralded photons to allow enough time for the switching electronics and the realization of fast, low-loss switches on the same platform.

Continuous variable — squeezed light sources. Theoretical progress towards establishing fault-tolerance thresholds for CV QIP[301,302] has renewed interest in the scalable integration of many squeezed light sources to produce large CV cluster states[243] (possibly with error correction) for universal quantum computation. Besides quantum computation, near-term algorithms such as Gaussian boson sampling for simulating molecular vibronic spectra also require the interference, control and detection of many squeezers[303]. A squeezed state has noise in one of its quadratures (that is, its amplitude or phase) reduced below the quantum shot noise limit, at the expense of higher noise in the orthogonal quadrature[304], as dictated by the Heisenberg uncertainty relation. Squeezed light enables quantum-enhanced sensing for detection below the standard quantum limit[305–308], as well as quantum communication. Additionally, by combining photonic circuits for mixing and manipulating these states with operations performed on these states, squeezed light can be used for QIP[250].

Although quantum technologies using squeezed light possess advantages such as deterministic generation using parametric nonlinearities and efficient detection using room-temperature p–i–n diodes[250,251], the development of on-chip squeezed light sources has historically lagged behind their single-photon counterparts. The same processes that produce photon pairs at low pump powers (degenerate FWM and PDC) also produce brighter quantum states such as squeezed light when pumped at much higher powers. In all resonator-based squeezers, the maximum output squeezing level (that is, the degree of quantum noise reduction) is limited by the degree of overcoupling (that is, the ratio of coupling loss to total loss) by the expression $S = Q_c/(Q_i + Q_c)$, and strongly overcoupled microresonators are beneficial[251,309,310]. Although FWM-based and PDC-based squeezing is highly sensitive to phase matching, squeezed light can also be generated using SPM, a process that is automatically phase-matched, as shown in fibres[311].

Integrated sources naturally produce squeezing over a large bandwidth (approximately gigahertz)[249,312] owing to their compact sizes and consequently broader resonance linewidths than their off-chip counterparts without requiring high pump powers[313]. Large bandwidths enable high-speed QIP, quantum key distribution and quantum communication[314]. Another major advantage of integrated CV QIP is the high visibility of homodyne interference afforded by waveguides owing to confinement in a well-defined spatial mode[315]. However, the degree of detected squeezing has been rather limited in high-confinement integrated platforms. Large squeezing levels are necessary for fault tolerance in QIP (with thresholds ~10 dB)[301,302], for quantum-enhanced metrology[305] and for high fidelity in CV quantum teleportation. Squeezing is especially fragile against losses, which degrade the quantum noise reduction by mixing the squeezed noise with vacuum noise and affecting the purity of the quantum state. Hence, mature low-loss platforms, such as SiO_2, Si_3N_4, LN and KTP, have been primarily investigated for squeezed light generation[251]. Emerging materials such as graphene and TMDs, which are predicted to have large nonlinearities[19,316], would need a reduced total device loss to below ~3 dB to observe detectable squeezing[316].

High squeezing levels typically require large parametric gain, and the current record for squeezing is 15 dB in off-chip KTP crystals[317]. Diffusion-fabricated structures such as LN waveguides[318,319] and cavities[309,310,320] and KTP waveguides[321] have generated squeezed light, with a maximum squeezing level of 5 dB (ref. 322). An impressive recent experiment incorporated two independent LN squeezers, photonic circuitry, thermo-optic phase shifters and homodyne interference on a single chip[315]. However, the low-index contrast of diffusion-fabricated waveguides leads to low confinement, centimetre-scale device lengths and large bending losses, making it challenging to scale up these sources or form travelling-wave cavities.

High-confinement platforms are a natural solution for the scalable integration of a large number of squeezers, beam splitters and homodyne interferometers to generate and detect entanglement. The first squeezing in high-confinement platforms was recorded in Si_3N_4 rings[249,323] using FWM parametric oscillation. However, the reported squeezing was accompanied by bright classical mean fields and by excess noise and did not directly produce the vacuum squeezing needed for several QIP protocols. In this context, a two-mode squeezed vacuum was generated in Si_3N_4 rings without detectable excess noise[324]. Alternatively, theoretical proposals[325] and preliminary experiments[312] have reported SPM-based squeezing using Si_3N_4 rings, but are limited to small squeezing levels owing to thermorefractive noise. SPM-based

devices, as opposed to singly pumped FWM devices, produce single-mode squeezing, which is often important for certain QIP protocols. Hence, several newer demonstrations have focused on dual-pump FWM squeezers to generate moderate levels (~2 dB) of single-mode squeezing[326–328].

A major near-term goal for on-chip squeezed light sources is to increase the level of squeezing as well as to incorporate a large number of them on chip, to be competitive with off-chip counterparts. However, a few applications could already benefit from the demonstrated low-to-moderate squeezing levels in current integrated platforms, such as secure quantum communications (2.51 dB)[329], and boson sampling for generating molecular vibronic spectra — a task that is challenging on classical computers[303,328]. Similar to the single-photon regime, in which spectral modes have been harnessed for quantum frequency combs, bulk $\chi^{(2)}$ cavities have generated multicolour entanglement using the frequency modes of a PDC comb[244,330]. In fact, the state of CV quantum combs is more advanced than single-photon quantum combs, as entanglement beyond the two-photon case as well as large-scale cluster-state generation has been realized in the CV regime off-chip[243,244,331], and a squeezed microcomb has been demonstrated in silica[332]. Non-centrosymmetric photonic materials including LN could potentially be used to integrate such ideas on chip in the near future. In fact, PDC in nanophotonic LN waveguides has reported ultrabroadband squeezing spanning 7 THz (ref. 333), as well as the highest level of on-chip squeezing ~4.9 dB spanning 25 THz (ref. 334), thus demonstrating the promise of nanophotonic LN for CV QIP.

Nonlinear-optic quantum logic gates and computing

Among the most intuitive schemes to implement optical quantum computing is the use of single-photon nonlinearities to realize two-qubit gates (such as CNOT or CPHASE) — a scheme called nonlinear optical quantum computing (NLOQC) in the discrete variable regime. Yet, the weakness of all-optical nonlinearities has made such a realization challenging, leading to the development of alternative schemes such as linear-optical quantum computing[335] to realize two-qubit gates, or measurement-based quantum computing using cluster states[301,336]. Hence, substantial efforts in photonics have focused on generating quantum sources of light to feed into LOQC or measurement-based quantum computing. Nevertheless, the probabilistic nature of such schemes[337,338] and the concomitant huge resource overheads to achieve fault tolerance[339] are important challenges to their practical realization. Hence, NLOQC remains one of the holy grails of photonics as it promises deterministic room-temperature operation.

Two-qubit entangling gates for NLOQC can be deterministically realized when the single-photon nonlinear coupling (g) between the interacting modes exceeds the dissipation rates (κ) of the modes — termed the 'strong coupling' regime ($g/\kappa > 1$). On the basis of strong spatial and spectral confinement, the highest reported values of g/κ have increased by several orders of magnitude from the early 2010s to 2022, from $<10^{-4}$ (ref. 340) to 1–1.5% in recent nanophotonic InGaP[41] and periodically poled LN[127] platforms. These efforts parallel the order of magnitude increase seen in SHG efficiency, now approaching $5 \times 10^6\%\ W^{-1}$. Partly inspired by experimental progress in nanophotonics, theoretical proposals that combine such strong nanophotonic confinement with other methods to enhance nonlinearities, such as temporal trapping or parametric amplification, have emerged for deterministic NLOQC[341–345]. Although these approaches exclusively use all-optical parametric nonlinearities, the combination of atoms with optical photons has successfully reached the strong coupling regime in off-chip platforms for some time now[346–349]. Integrating atom–photon coupling on-chip[350] offers another approach for deterministic two-qubit gates, albeit requiring more complicated setups to trap and coherently manipulate atoms.

Conclusions and perspective

High-confinement waveguides and resonators have been a game-changer for nonlinear optics, enabling phenomena that were previously inaccessible in fibre optics or bulk tabletop systems. Now that several nonlinear photonics platforms have achieved extremely low loss and high material quality, we expect these platforms to be key enablers for the major goals of the field including broadband classical and quantum frequency conversion, microresonator frequency-comb generation, quantum light sources and nonlinear optical quantum logic gates. Owing to their integration capability, these platforms are expected to be readily combined with systems of increasing complexity that have multiple linear and nonlinear functionalities. Traditional materials such as LN, silicon and silicon nitride are already being used in emerging applications. Specifically, periodic poling realized in nanophotonic high-confinement LN has shown low loss, ultra-high-speed modulation and significant $\chi^{(2)}$ nonlinearities. Hence, it is promising for quantum light sources to generate single photons and squeezed light as well as actively switched and/or multiplexed sources and multipartite entanglement in high dimensions. Further research on novel materials (such as 2D materials) is needed to improve material quality and integration capability, to enable complementary functionalities, enhance nonlinear effects or add tunability to traditional materials, opening opportunities for future applications. In addition to material developments, new device design approaches, such as inverse design through gradient-based optimization[351,352], or fundamental physics ideas, for example, bound states in the continuum or topology[353], have emerged for efficient nanoscale SHG[354,355] and for applications such as non-reciprocal LiDAR[351]. Similarly, the resurgence of unconventional optical computing and photonic neural networks necessitates novel designs for solving hard optimization problems[356] or accelerating machine-learning hardware, respectively. Hence, there is plenty of room to push the performance of nonlinear nanophotonic devices through progress in materials and devices for unprecedented quantum and classical technologies.

Published online: 1 May 2024

References

1. Foster, M. A. et al. Broad-band optical parametric gain on a silicon photonic chip. *Nature* **441**, 960–963 (2006).
   This work reports broadband phase-matched four-wave mixing optical amplification and frequency conversion in a silicon photonic chip through waveguide dispersion engineering.
2. Griffith, A. G. et al. Silicon-chip mid-infrared frequency comb generation. *Nat. Commun.* **6**, 6299 (2015).
3. Bell, B. A., He, J., Xiong, C. & Eggleton, B. J. Frequency conversion in silicon in the single photon regime. *Opt. Express* **24**, 5235–5242 (2016).
4. Yamada, H. et al. Nonlinear-optic silicon-nanowire waveguides. *Jpn. J. Appl. Phys.* **44**, 6541–6545 (2005).
5. Sederberg, S., Firby, C. J. & Elezzabi, A. Y. Efficient, broadband third-harmonic generation in silicon nanophotonic waveguides spectrally shaped by nonlinear propagation. *Opt. Express* **27**, 4990–5004 (2019).
6. Timurdogan, E., Poulton, C. V., Byrd, M. J. & Watts, M. R. Electric field-induced second-order nonlinear optical effects in silicon waveguides. *Nat. Photon.* **11**, 200–206 (2017).
7. Wang, C. et al. Integrated lithium niobate electro-optic modulators operating at CMOS-compatible voltages. *Nature* **562**, 101 (2018).
8. Zhang, M. et al. Electronically programmable photonic molecule. *Nat. Photon.* **13**, 36 (2019).
9. Kippenberg, T. J., Gaeta, A. L., Lipson, M. & Gorodetsky, M. L. Dissipative Kerr solitons in optical microresonators. *Science* **361**, eaan8083 (2018).

10. Brasch, V. et al. Photonic chip-based optical frequency comb using soliton Cherenkov radiation. *Science* **351**, 357–360 (2016).
11. Yang, K. Y. et al. Bridging ultrahigh-*Q* devices and photonic circuits. *Nat. Photon.* **12**, 297–302 (2018).
12. Moss, D. J., Morandotti, R., Gaeta, A. L. & Lipson, M. New CMOS-compatible platforms based on silicon nitride and Hydex for nonlinear optics. *Nat. Photon.* **7**, 597–607 (2013).
13. Pu, M., Ottaviano, L., Semenova, E. & Yvind, K. Efficient frequency comb generation in AlGaAs-on-insulator. *Optica* **3**, 823–826 (2016).
14. Hausmann, B. J. M., Bulu, I., Venkataraman, V., Deotare, P. & Lončar, M. Diamond nonlinear photonics. *Nat. Photon.* **8**, 369–374 (2014).
15. Lukin, D. M. et al. 4H-silicon-carbide-on-insulator for integrated quantum and nonlinear photonics. *Nat. Photon.* **14**, 330–334 (2020).
16. Cai, L., Li, J., Wang, R. & Li, Q. Octave-spanning microcomb generation in 4H-silicon-carbide-on-insulator photonics platform. *Photon. Res.* **10**, 870–876 (2022).
17. Cardenas, J. et al. Optical nonlinearities in high-confinement silicon carbide waveguides. *Opt. Lett.* **40**, 4138 (2015).
18. Yin, X. et al. Edge nonlinear optics on a MoS_2 atomic monolayer. *Science* **344**, 488–490 (2014).
19. Gu, T. et al. Regenerative oscillation and four-wave mixing in graphene optoelectronics. *Nat. Photon.* **6**, 554–559 (2012).
20. Hendry, E., Hale, P. J., Moger, J., Savchenko, A. K. & Mikhailov, S. A. Coherent nonlinear optical response of graphene. *Phys. Rev. Lett.* **105**, 097401 (2010).
21. Joshi, C., Farsi, A., Clemmen, S., Ramelow, S. & Gaeta, A. L. Frequency multiplexing for quasi-deterministic heralded single-photon sources. *Nat. Commun.* **9**, 847 (2018).
22. Lu, H.-H. et al. Electro-optic frequency beam splitters and tritters for high-fidelity photonic quantum information processing. *Phys. Rev. Lett.* **120**, 030502 (2018).
23. Reimer, C. et al. Generation of multiphoton entangled quantum states by means of integrated frequency combs. *Science* **351**, 1176–1180 (2016).
This work extends Kerr frequency comb platforms to the discrete-variable quantum regime to demonstrate complex quantum optical states showing multiphoton entanglement.
24. Kues, M. et al. On-chip generation of high-dimensional entangled quantum states and their coherent control. *Nature* **546**, 622–626 (2017).
25. Guidry, M. A., Lukin, D. M., Yang, K. Y., Trivedi, R. & Vučković, J. Quantum optics of soliton microcombs. *Nat. Photon.* **16**, 52–58 (2022).
26. Stern, B., Ji, X., Okawachi, Y., Gaeta, A. L. & Lipson, M. Battery-operated integrated frequency comb generator. *Nature* **562**, 401 (2018).
This paper presents the first demonstration of an external-power-source-free Kerr frequency comb powered by a battery, including low-noise soliton states.
27. Trocha, P. et al. Ultrafast optical ranging using microresonator soliton frequency combs. *Science* **359**, 887–891 (2018).
28. Suh, M.-G. & Vahala, K. J. Soliton microcomb range measurement. *Science* **359**, 884–887 (2018).
This work presents a microresonator frequency comb used to parallelize a LiDAR measurement of distance and velocity.
29. Suh, M.-G., Yang, Q.-F., Yang, K. Y., Yi, X. & Vahala, K. J. Microresonator soliton dual-comb spectroscopy. *Science* **354**, 600–603 (2016).
30. Yang, K. Y. et al. Broadband dispersion-engineered microresonator on a chip. *Nat. Photon.* **10**, 316–320 (2016).
This paper presents precise higher-order dispersion control in wedge resonators with quality factors above 100 million, which is important for low-power nonlinear optics.
31. Ji, X. et al. Ultra-low-loss on-chip resonators with sub-milliwatt parametric oscillation threshold. *Optica* **4**, 619 (2017).
In this work, high-quality factors of up to 67 million in high-confinement silicon nitride resonators are achieved by substantially reducing the surface roughness of the waveguide.
32. Spencer, D. T., Bauters, J. F., Heck, M. J. R. & Bowers, J. E. Integrated waveguide coupled Si_3N_4 resonators in the ultrahigh-*Q* regime. *Optica* **1**, 153–157 (2014).
33. Pfeiffer, M. H. P. et al. Ultra-smooth silicon nitride waveguides based on the Damascene reflow process: fabrication and loss origins. *Optica* **5**, 884–892 (2018).
34. Liu, K. et al. Ultralow 0.034 dB/m loss wafer-scale integrated photonics realizing 720 million Q and 380 μW threshold Brillouin lasing. *Opt. Lett.* **47**, 1855–1858 (2022).
35. Foster, M. A., Turner, A. C., Lipson, M. & Gaeta, A. L. Nonlinear optics in photonic nanowires. *Opt. Express* **16**, 1300–1320 (2008).
36. Levy, J. S. et al. CMOS-compatible multiple-wavelength oscillator for on-chip optical interconnects. *Nat. Photon.* **4**, 37–40 (2010).
37. Razzari, L. et al. CMOS-compatible integrated optical hyper-parametric oscillator. *Nat. Photon.* **4**, 41–45 (2010).
38. Xie, W. et al. Ultrahigh-*Q* AlGaAs-on-insulator microresonators for integrated nonlinear photonics. *Opt. Express* **28**, 32894 (2020).
A low threshold of <120 μW for frequency-comb generation is achieved in AlGaAs microresonators with quality factor greater than 10^6.
39. Boyd, R. W. *Nonlinear Optics* (Academic Press, 2008).
40. Sipe, J. E., Moss, D. J. & van Driel, H. M. Phenomenological theory of optical second- and third-harmonic generation from cubic centrosymmetric crystals. *Phys. Rev. B* **35**, 1129–1141 (1987).
41. Zhao, M. & Fang, K. InGaP quantum nanophotonic integrated circuits with 1.5% nonlinearity-to-loss ratio. *Optica* **9**, 258 (2022).
This paper holds the current record for the highest nonlinearity-to-loss ratio in solid-state parametric nonlinear optical platforms.
42. Jung, H., Xiong, C., Fong, K. Y., Zhang, X. & Tang, H. X. Optical frequency comb generation from aluminum nitride microring resonator. *Opt. Lett.* **38**, 2810–2813 (2013).
43. Liu, X. et al. Aluminum nitride nanophotonics for beyond-octave soliton microcomb generation and self-referencing. *Nat. Commun.* **12**, 5428 (2021).
44. Chen, J.-Y. et al. Ultra-efficient frequency conversion in quasi-phase-matched lithium niobate microrings. *Optica* **6**, 1244–1245 (2019).
45. Eggleton, B. J., Poulton, C. G., Rakich, P. T., Steel, M. J. & Bahl, G. Brillouin integrated photonics. *Nat. Photon.* **13**, 664–677 (2019).
46. Raza, A. et al. High index contrast photonic platforms for on-chip Raman spectroscopy. *Opt. Express* **27**, 23067–23079 (2019).
47. Mizrahi, V., DeLong, K. W., Stegeman, G. I., Saifi, M. A. & Andrejco, M. J. Two-photon absorption as a limitation to all-optical switching. *Opt. Lett.* **14**, 1140–1142 (1989).
48. Miller, S. A. et al. Low-loss silicon platform for broadband mid-infrared photonics. *Optica* **4**, 707–712 (2017).
49. Engin, E. et al. Photon pair generation in a silicon micro-ring resonator with reverse bias enhancement. *Opt. Express* **21**, 27826–27834 (2013).
50. Xuan, Y. et al. High-*Q* silicon nitride microresonators exhibiting low-power frequency comb initiation. *Optica* **3**, 1171–1180 (2016).
51. Xie, S., Zhang, Y., Hu, Y., Veilleux, S. & Dagenais, M. On-chip Fabry–Perot Bragg grating cavity enhanced four-wave mixing. *ACS Photon.* **7**, 1009–1015 (2020).
52. El Dirani, H. et al. Annealing-free Si_3N_4 frequency combs for monolithic integration with Si photonics. *Appl. Phys. Lett.* **113**, 081102 (2018).
53. Luke, K., Dutt, A., Poitras, C. B. & Lipson, M. Overcoming Si_3N_4 film stress limitations for high quality factor ring resonators. *Opt. Express* **21**, 22829–22833 (2013).
In this work, thick (>700 nm), crack-free films of silicon nitride are deposited, enabling anomalous dispersion for high-confinement nonlinear applications.
54. Pfeiffer, M. H. P. et al. Photonic Damascene process for integrated high-Q microresonator based nonlinear photonics. *Optica* **3**, 20–25 (2016).
This paper reports the first usage of the Damascene process for silicon nitride waveguides, enabling the fabrication of thicker waveguides by overcoming film stress challenges.
55. Ye, Z., Fülöp, A., Helgason, Ó. B., Andrekson, P. A. & Torres-Company, V. Low-loss high-Q silicon-rich silicon nitride microresonators for Kerr nonlinear optics. *Opt. Lett.* **44**, 3326–3329 (2019).
56. Chia, X. X. et al. Low-power four-wave mixing in deuterated silicon-rich nitride ring resonators. *J. Lightwave Technol.* **41**, 3115–3130 (2023).
57. Li, K., Sun, H. & Foster, A. C. Four-wave mixing Bragg scattering in hydrogenated amorphous silicon waveguides. *Opt. Lett.* **42**, 1488–1491 (2017).
58. Dave, U. D. et al. Telecom to mid-infrared spanning supercontinuum generation in hydrogenated amorphous silicon waveguides using a thulium doped fiber laser pump source. *Opt. Express* **21**, 32032–32039 (2013).
59. Safioui, J. et al. Supercontinuum generation in hydrogenated amorphous silicon waveguides at telecommunication wavelengths. *Opt. Express* **22**, 3089–3097 (2014).
60. Wang, K.-Y. & Foster, A. C. Ultralow power continuous-wave frequency conversion in hydrogenated amorphous silicon waveguides. *Opt. Lett.* **37**, 1331–1333 (2012).
61. Grillet, C. et al. Amorphous silicon nanowires combining high nonlinearity, FOM and optical stability. *Opt. Express* **20**, 22609–22615 (2012).
62. Xiao, T.-H. et al. Mid-infrared high-*Q* germanium microring resonator. *Opt. Lett.* **43**, 2885–2888 (2018).
63. Carletti, L. et al. Nonlinear optical response of low loss silicon germanium waveguides in the mid-infrared. *Opt. Express* **23**, 8261–8271 (2015).
64. Sinobad, M. et al. Mid-infrared octave spanning supercontinuum generation to 8.5 μm in silicon–germanium waveguides. *Optica* **5**, 360–366 (2018).
65. Wu, X., Fan, T., Eftekhar, A. A. & Adibi, A. High-*Q* microresonators integrated with microheaters on a 3C-SiC-on-insulator platform. *Opt. Lett.* **44**, 4941–4944 (2019).
66. Lu, X., Lee, J. Y., Feng, P. X.-L. & Lin, Q. High Q silicon carbide microdisk resonator. *Appl. Phys. Lett.* **104**, 181103 (2014).
67. Hausmann, B. J. M. et al. Integrated high-quality factor optical resonators in diamond. *Nano Lett.* **13**, 1898–1902 (2013).
68. Wang, C. et al. High-Q microresonators on 4H-silicon-carbide-on-insulator platform for nonlinear photonics. *Light Sci. Appl.* **10**, 139 (2021).
69. Guidry, M. A. et al. Optical parametric oscillation in silicon carbide nanophotonics. *Optica* **7**, 1139–1142 (2020).
70. Li, J., Wang, R., Cai, L. & Li, Q. Measurement of the Kerr nonlinear refractive index and its variation among 4H-SiC wafers. *Phys. Rev. Appl.* **19**, 034083 (2023).
71. Liang, D. & Bowers, J. E. Recent progress in heterogeneous III–V-on-silicon photonic integration. *Light Adv. Manuf.* **2**, 59–83 (2021).
72. Duan, G.-H. et al. Hybrid III–V on silicon lasers for photonic integrated circuits on silicon. *IEEE J. Sel. Top. Quantum Electron.* **20**, 158–170 (2014).
73. Kultavewuti, P., Pusino, V., Sorel, M. & Aitchison, J. S. Low-power continuous-wave four-wave mixing wavelength conversion in AlGaAs-nanowaveguide microresonators. *Opt. Lett.* **40**, 3029–3032 (2015).
74. Sarrafi, P. et al. Continuous-wave quasi-phase-matched waveguide correlated photon pair source on a III–V chip. *Appl. Phys. Lett.* **103**, 251115 (2013).
75. Aitchison, J. S., Hutchings, D. C., Kang, J. U., Stegeman, G. I. & Villeneuve, A. The nonlinear optical properties of AlGaAs at the half band gap. *IEEE J. Quantum Electron.* **33**, 341–348 (1997).
76. Pu, M. et al. Ultra-efficient and broadband nonlinear AlGaAs-on-insulator chip for low-power optical signal processing. *Laser Photon. Rev.* **12**, 1800111 (2018).

77. Liu, X. et al. Ultra-high-Q UV microring resonators based on a single-crystalline AlN platform. *Optica* **5**, 1279–1282 (2018).
78. Troha, T. et al. UV second harmonic generation in AlN waveguides with modal phase matching. *Opt. Mater. Express* **6**, 2014–2023 (2016).
79. Lu, T.-J. et al. Aluminum nitride integrated photonics platform for the ultraviolet to visible spectrum. *Opt. Express* **26**, 11147–11160 (2018).
80. Guo, X., Zou, C.-L., Jung, H. & Tang, H. X. On-chip strong coupling and efficient frequency conversion between telecom and visible optical modes. *Phys. Rev. Lett.* **117**, 123902 (2016).
81. Surya, J. B., Guo, X., Zou, C.-L. & Tang, H. X. Efficient third-harmonic generation in composite aluminum nitride/silicon nitride microrings. *Optica* **5**, 103–108 (2018).
82. Jung, H., Stoll, R., Guo, X., Fischer, D. & Tang, H. X. Green, red, and IR frequency comb line generation from single IR pump in AlN microring resonator. *Optica* **1**, 396–399 (2014).
83. Zhang, M., Wang, C., Cheng, R., Shams-Ansari, A. & Lončar, M. Monolithic ultra-high-Q lithium niobate microring resonator. *Optica* **4**, 1536 (2017).
This work demonstrates a hundred times improvement in quality factors (reaching 10 million), in thin-film lithium niobate ring resonators through optimized etching processes that reduced surface roughness.
84. Xu, Y. et al. Mitigating photorefractive effect in thin-film lithium niobate microring resonators. *Opt. Express* **29**, 5497–5504 (2021).
85. Lee, H. et al. Chemically etched ultrahigh-Q wedge-resonator on a silicon chip. *Nat. Photon.* **6**, 369–373 (2012).
86. Eggleton, B. J., Luther-Davies, B. & Richardson, K. Chalcogenide photonics. *Nat. Photon.* **5**, 141–148 (2011).
87. Haffner, C. et al. Low-loss plasmon-assisted electro-optic modulator. *Nature* **556**, 483 (2018).
88. Ummethala, S. et al. THz-to-optical conversion in wireless communications using an ultra-broadband plasmonic modulator. *Nat. Photon.* **13**, 519–524 (2019).
89. Alexander, K. et al. Nanophotonic Pockels modulators on a silicon nitride platform. *Nat. Commun.* **9**, 3444 (2018).
90. Abel, S. et al. Large Pockels effect in micro- and nanostructured barium titanate integrated on silicon. *Nat. Mater.* **18**, 42 (2019).
91. Hong, S.-Y. et al. Optical third-harmonic generation in graphene. *Phys. Rev. X* **3**, 021014 (2013).
92. Soavi, G. et al. Broadband, electrically tunable third-harmonic generation in graphene. *Nat. Nanotechnol.* **13**, 583–588 (2018).
93. Kumar, N. et al. Third harmonic generation in graphene and few-layer graphite films. *Phys. Rev. B* **87**, 121406 (2013).
94. Wang, Z. et al. Evidence of high-temperature exciton condensation in two-dimensional atomic double layers. *Nature* **574**, 76–80 (2019).
95. Wu, J., Lin, H., Moss, D. J., Loh, K. P. & Jia, B. Graphene oxide for photonics, electronics and optoelectronics. *Nat. Rev. Chem.* **7**, 162–183 (2023).
96. Fryett, T., Zhan, A. & Majumdar, A. Cavity nonlinear optics with layered materials. *Nanophotonics* **7**, 355–370 (2018).
97. Autere, A. et al. Nonlinear optics with 2D layered materials. *Adv. Mater.* **30**, 1705963 (2018).
98. Vermeulen, N. et al. Post-2000 nonlinear optical materials and measurements: data tables and best practices. *J. Phys. Photon.* **5**, 035001 (2023).
99. Hwang, A. Y. et al. Mid-infrared spectroscopy with a broadly tunable thin-film lithium niobate optical parametric oscillator. *Optica* **10**, 1535–1542 (2023).
100. Wu, B., Chen, N., Chen, C., Deng, D. & Xu, Z. Highly efficient ultraviolet generation at 355 nm in LiB_3O_5. *Opt. Lett.* **14**, 1080–1081 (1989).
101. Zhao, Y., Lombardo, D., Mathews, J. & Agha, I. All-optical switching via four-wave mixing Bragg scattering in a silicon platform. *APL Photon.* **2**, 026102 (2017).
102. Barad, Y., Eisenberg, H., Horowitz, M. & Silberberg, Y. Nonlinear scanning laser microscopy by third harmonic generation. *Appl. Phys. Lett.* **70**, 922–924 (1997).
103. Lau, R. K. W. et al. Continuous-wave mid-infrared frequency conversion in silicon nanowaveguides. *Opt. Lett.* **36**, 1263–1265 (2011).
104. Lu, X. et al. Efficient telecom-to-visible spectral translation through ultralow power nonlinear nanophotonics. *Nat. Photon.* **13**, 593–601 (2019).
105. Spencer, D. T. et al. An optical-frequency synthesizer using integrated photonics. *Nature* **557**, 81 (2018).
This paper reports a key milestone in synthesizing arbitrary optical frequencies using self-referenced combs based on two disparate platforms — Si_3N_4 and SiO_2.
106. Sutherland, R. L., McLean, D. G. & Kirkpatrick, S. *Handbook of Nonlinear Optics* (Marcel Dekker, 2003).
107. Wang, C. et al. Ultrahigh-efficiency wavelength conversion in nanophotonic periodically poled lithium niobate waveguides. *Optica* **5**, 1438–1441 (2018).
108. Corcoran, B. et al. Green light emission in silicon through slow-light enhanced third-harmonic generation in photonic-crystal waveguides. *Nat. Photon.* **3**, 206–210 (2009).
109. Chang, L. et al. Heterogeneously integrated GaAs waveguides on insulator for efficient frequency conversion. *Laser Photon. Rev.* **12**, 1800149 (2018).
110. Sayem, A. A. et al. Efficient and tunable blue light generation using lithium niobate nonlinear photonics. *Appl. Phys. Lett.* **119**, 231104 (2021).
111. Park, T. et al. High-efficiency second harmonic generation of blue light on thin-film lithium niobate. *Opt. Lett.* **47**, 2706–2709 (2022).
112. Luo, R., He, Y., Liang, H., Li, M. & Lin, Q. Semi-nonlinear nanophotonic waveguides for highly efficient second-harmonic generation. *Laser Photon. Rev.* **13**, 1800288 (2019).
113. Luo, R., He, Y., Liang, H., Li, M. & Lin, Q. Highly tunable efficient second-harmonic generation in a lithium niobate nanophotonic waveguide. *Optica* **5**, 1006–1011 (2018).
114. Zhao, J. et al. Shallow-etched thin-film lithium niobate waveguides for highly-efficient second-harmonic generation. *Opt. Express* **28**, 19669–19682 (2020).
115. Wang, C. et al. Metasurface-assisted phase-matching-free second harmonic generation in lithium niobate waveguides. *Nat. Commun.* **8**, 2098 (2017).
116. Levy, J. S., Foster, M. A., Gaeta, A. L. & Lipson, M. Harmonic generation in silicon nitride ring resonators. *Opt. Express* **19**, 11415–11421 (2011).
117. Billat, A. et al. Large second harmonic generation enhancement in Si_3N_4 waveguides by all-optically induced quasi-phase-matching. *Nat. Commun.* **8**, 1016 (2017).
118. Nitiss, E. et al. Formation rules and dynamics of photoinduced $\chi^{(2)}$ gratings in silicon nitride waveguides. *ACS Photon.* **7**, 147–153 (2020).
119. Grassani, D., Pfeiffer, M. H. P., Kippenberg, T. J. & Brès, C.-S. Second- and third-order nonlinear wavelength conversion in an all-optically poled Si_3N_4 waveguide. *Opt. Lett.* **44**, 106–109 (2019).
120. Hickstein, D. D. et al. Self-organized nonlinear gratings for ultrafast nanophotonics. *Nat. Photon.* **13**, 494–499 (2019).
121. Nitiss, E., Hu, J., Stroganov, A. & Brès, C.-S. Optically reconfigurable quasi-phase-matching in silicon nitride microresonators. *Nat. Photon.* **16**, 134–141 (2022).
This work shows optically reconfigurable quasi-phase-matching in silicon nitride using the photogalvanic effect within a microresonator, enabling high second-harmonic generation conversion efficiency through an effective $\chi^{(2)}$.
122. Logan, A. D. et al. 400%/W second harmonic conversion efficiency in 14 μm-diameter gallium phosphide-on-oxide resonators. *Opt. Express* **26**, 33687–33699 (2018).
123. Lake, D. P. et al. Efficient telecom to visible wavelength conversion in doubly resonant gallium phosphide microdisks. *Appl. Phys. Lett.* **108**, 031109 (2016).
124. Bruch, A. W. et al. 17 000%/W second-harmonic conversion efficiency in single-crystalline aluminum nitride microresonators. *Appl. Phys. Lett.* **113**, 131102 (2018).
125. Lin, J. et al. Broadband quasi-phase-matched harmonic generation in an on-chip monocrystalline lithium niobate microdisk resonator. *Phys. Rev. Lett.* **122**, 173903 (2019).
126. May, S., Kues, M., Clerici, M. & Sorel, M. Second-harmonic generation in AlGaAs-on-insulator waveguides. *Opt. Lett.* **44**, 1339–1342 (2019).
127. Lu, J., Li, M., Zou, C.-L., Sayem, A. A. & Tang, H. X. Toward 1% single-photon anharmonicity with periodically poled lithium niobate microring resonators. *Optica* **7**, 1654–1659 (2020).
This paper demonstrates a record high conversion efficiency of 5,000,000% W^{-1} from the telecom band to 752 nm in a periodically poled thin-film lithium niobate microresonator.
128. Soref, R. Mid-infrared photonics in silicon and germanium. *Nat. Photon.* **4**, 495–497 (2010).
129. Mishra, J. et al. Mid-infrared nonlinear optics in thin-film lithium niobate on sapphire. *Optica* **8**, 921–924 (2021).
130. McKenna, T. P. et al. Ultra-low-power second-order nonlinear optics on a chip. *Nat. Commun.* **13**, 4532 (2022).
131. Roy, A. et al. Visible-to-mid-IR tunable frequency comb in nanophotonics. *Nat. Commun.* **14**, 6549 (2023).
132. Liu, X., Osgood, R. M. Jr, Vlasov, Y. A. & Green, W. M. J. Mid-infrared optical parametric amplifier using silicon nanophotonic waveguides. *Nat. Photon.* **4**, 557–560 (2010).
133. Zlatanovic, S. et al. Mid-infrared wavelength conversion in silicon waveguides using ultracompact telecom-band-derived pump source. *Nat. Photon.* **4**, 561–564 (2010).
134. Sahin, E. et al. Difference-frequency generation in optically poled silicon nitride waveguides. *Nanophotonics* **10**, 1923–1930 (2021).
135. Liu, X. et al. Bridging the mid-infrared-to-telecom gap with silicon nanophotonic spectral translation. *Nat. Photon.* **6**, 667–671 (2012).
136. Stievater, T. H. et al. Mid-infrared difference-frequency generation in suspended GaAs waveguides. *Opt. Lett.* **39**, 945–948 (2014).
This paper presents the generation of mid-infrared light up to 3,150 nm in suspended GaAs waveguides using difference frequency generation.
137. Tanzilli, S. et al. A photonic quantum information interface. *Nature* **437**, 116 (2005).
138. Soltani, M. et al. Efficient quantum microwave-to-optical conversion using electro-optic nanophotonic coupled resonators. *Phys. Rev. A* **96**, 043808 (2017).
139. Li, Q., Davanço, M. & Srinivasan, K. Efficient and low-noise single-photon-level frequency conversion interfaces using silicon nanophotonics. *Nat. Photon.* **10**, 406–414 (2016).
This work provides among the first reports of on-chip nonlinear optical frequency conversion at the single-photon level, using four-wave mixing Bragg scattering in silicon nitride.
140. Dautet, H. et al. Photon counting techniques with silicon avalanche photodiodes. *Appl. Opt.* **32**, 3894–3900 (1993).
141. Kumar, P. Quantum frequency conversion. *Opt. Lett.* **15**, 1476–1478 (1990).
142. McGuinness, H. J., Raymer, M. G., McKinstrie, C. J. & Radic, S. Quantum frequency translation of single-photon states in a photonic crystal fiber. *Phys. Rev. Lett.* **105**, 093604 (2010).
143. McKinstrie, C. J., Yu, M., Raymer, M. G. & Radic, S. Quantum noise properties of parametric processes. *Opt. Express* **13**, 4986 (2005).
144. Agrawal, G. P. *Nonlinear Fiber Optics* (Elsevier/Academic Press, 2013).
145. Albota, M. A. & Wong, F. N. C. Efficient single-photon counting at 1.55 μm by means of frequency upconversion. *Opt. Lett.* **29**, 1449–1451 (2004).
146. Vandevender, A. P. & Kwiat, P. G. High efficiency single photon detection via frequency up-conversion. *J. Mod. Opt.* **51**, 1433–1445 (2004).

147. Huang, J. & Kumar, P. Observation of quantum frequency conversion. *Phys. Rev. Lett.* **68**, 2153–2156 (1992).
148. Ramelow, S., Fedrizzi, A., Poppe, A., Langford, N. K. & Zeilinger, A. Polarization-entanglement-conserving frequency conversion of photons. *Phys. Rev. A* **85**, 013845 (2012).
149. Ates, S. et al. Two-photon interference using background-free quantum frequency conversion of single photons emitted by an InAs quantum dot. *Phys. Rev. Lett.* **109**, 147405 (2012).
150. Allgaier, M. et al. Highly efficient frequency conversion with bandwidth compression of quantum light. *Nat. Commun.* **8**, 14288 (2017).
151. Rütz, H., Luo, K.-H., Suche, H. & Silberhorn, C. Quantum frequency conversion between infrared and ultraviolet. *Phys. Rev. Appl.* **7**, 024021 (2017).
152. Maring, N., Lago-Rivera, D., Lenhard, A., Heinze, G. & Riedmatten, Hde Quantum frequency conversion of memory-compatible single photons from 606 nm to the telecom C-band. *Optica* **5**, 507–513 (2018).
153. Rakher, M. T., Ma, L., Slattery, O., Tang, X. & Srinivasan, K. Quantum transduction of telecommunications-band single photons from a quantum dot by frequency upconversion. *Nat. Photon.* **4**, 786–791 (2010).
154. Zaske, S. et al. Visible-to-telecom quantum frequency conversion of light from a single quantum emitter. *Phys. Rev. Lett.* **109**, 147404 (2012).
155. Weber, J. H. et al. Two-photon interference in the telecom C-band after frequency conversion of photons from remote quantum emitters. *Nat. Nanotechnol.* **14**, 23 (2019).
156. Ikuta, R. et al. Wide-band quantum interface for visible-to-telecommunication wavelength conversion. *Nat. Commun.* **2**, 537 (2011).
157. De Greve, K. et al. Quantum-dot spin–photon entanglement via frequency downconversion to telecom wavelength. *Nature* **491**, 421–425 (2012).
158. Manurkar, P. et al. Multidimensional mode-separable frequency conversion for high-speed quantum communication. *Optica* **3**, 1300–1307 (2016).
159. Albrecht, B., Farrera, P., Fernandez-Gonzalvo, X., Cristiani, M. & de Riedmatten, H. A waveguide frequency converter connecting rubidium-based quantum memories to the telecom C-band. *Nat. Commun.* **5**, 3376 (2014).
160. Kobayashi, T. et al. Frequency-domain Hong–Ou–Mandel interference. *Nat. Photon.* **10**, 441–444 (2016).
161. Singh, A. et al. Quantum frequency conversion of a quantum dot single-photon source on a nanophotonic chip. *Optica* **6**, 563–569 (2019).
162. Langrock, C. et al. Highly efficient single-photon detection at communication wavelengths by use of upconversion in reverse-proton-exchanged periodically poled $LiNbO_3$ waveguides. *Opt. Lett.* **30**, 1725–1727 (2005).
163. Clemmen, S., Farsi, A., Ramelow, S. & Gaeta, A. L. Ramsey interference with single photons. *Phys. Rev. Lett.* **117**, 223601 (2016).
164. Clark, A. S., Shahnia, S., Collins, M. J., Xiong, C. & Eggleton, B. J. High-efficiency frequency conversion in the single-photon regime. *Opt. Lett.* **38**, 947–949 (2013).
165. Chen, J.-Y. et al. Photon conversion and interaction in a quasi-phase-matched microresonator. *Phys. Rev. Appl.* **16**, 064004 (2021).
166. Moille, G. et al. Ultra-broadband Kerr microcomb through soliton spectral translation. *Nat. Commun.* **12**, 7275 (2021).
167. Ramelow, S. et al. Strong nonlinear coupling in a Si_3N_4 ring resonator. *Phys. Rev. Lett.* **122**, 153906 (2019).
168. Zhao, Y., Jang, J. K., Okawachi, Y. & Gaeta, A. L. Theory of $\chi^{(2)}$-microresonator-based frequency conversion. *Opt. Lett.* **46**, 5393–5396 (2021).
169. Heuck, M. et al. Unidirectional frequency conversion in microring resonators for on-chip frequency-multiplexed single-photon sources. *N. J. Phys.* **21**, 033037 (2019).
170. Ji, X. et al. On-chip tunable photonic delay line. *APL Photon.* **4**, 090803 (2019).
171. Bell, B. A., Xiong, C., Marpaung, D., McKinstrie, C. J. & Eggleton, B. J. Uni-directional wavelength conversion in silicon using four-wave mixing driven by cross-polarized pumps. *Opt. Lett.* **42**, 1668 (2017).
172. Bahar, E., Ding, X., Dahan, A., Suchowski, H. & Moses, J. Adiabatic four-wave mixing frequency conversion. *Opt. Express* **26**, 25582–25601 (2018).
173. Lemos, G. B. et al. Quantum imaging with undetected photons. *Nature* **512**, 409–412 (2014).
174. Kalashnikov, D. A., Paterova, A. V., Kulik, S. P. & Krivitsky, L. A. Infrared spectroscopy with visible light. *Nat. Photon.* **10**, 98–101 (2016).
175. Riemensberger, J. et al. Massively parallel coherent laser ranging using a soliton microcomb. *Nature* **581**, 164–170 (2020).
This work presents a microresonator frequency comb used to parallelize a LiDAR measurement of distance and velocity.
176. Dutt, A. et al. On-chip dual-comb source for spectroscopy. *Sci. Adv.* **4**, e1701858 (2018).
177. Yu, M. et al. Silicon-chip-based mid-infrared dual-comb spectroscopy. *Nat. Commun.* **9**, 1869 (2018).
178. Marin-Palomo, P. et al. Microresonator-based solitons for massively parallel coherent optical communications. *Nature* **546**, 274–279 (2017).
179. Rizzo, A. et al. Petabit-scale silicon photonic interconnects with integrated kerr frequency combs. *IEEE J. Sel. Top. Quantum Electron*. https://doi.org/10.1109/JSTQE.2022.3197375 (2022).
180. Yang, K. Y. et al. Multi-dimensional data transmission using inverse-designed silicon photonics and microcombs. *Nat. Commun.* **13**, 7862 (2022).
181. Ji, X. et al. Chip-based frequency comb sources for optical coherence tomography. *Opt. Express* **27**, 19896–19905 (2019).
182. Marchand, P. J. et al. Soliton microcomb based spectral domain optical coherence tomography. *Nat. Commun.* **12**, 427 (2021).
183. Suh, M.-G. et al. Searching for exoplanets using a microresonator astrocomb. *Nat. Photon.* **13**, 25 (2019).
184. Obrzud, E. et al. A microphotonic astrocomb. *Nat. Photon.* **13**, 31 (2019).
185. Del'Haye, P. et al. Optical frequency comb generation from a monolithic microresonator. *Nature* **450**, 1214–1217 (2007).
186. Gaeta, A. L., Lipson, M. & Kippenberg, T. J. Photonic-chip-based frequency combs. *Nat. Photon.* **13**, 158 (2019).
187. Zhang, M. et al. Broadband electro-optic frequency comb generation in a lithium niobate microring resonator. *Nature* **568**, 373–377 (2019).
188. Rueda, A., Sedlmeir, F., Kumari, M., Leuchs, G. & Schwefel, H. G. L. Resonant electro-optic frequency comb. *Nature* **568**, 378 (2019).
189. Nagarjun, K. P., Jeyaselvan, V., Selvaraja, S. K. & Supradeepa, V. R. Generation of tunable, high repetition rate optical frequency combs using on-chip silicon modulators. *Opt. Express* **26**, 10744–10753 (2018).
190. Savchenkov, A. A. et al. Low threshold optical oscillations in a whispering gallery mode CaF_2 resonator. *Phys. Rev. Lett.* **93**, 243905 (2004).
191. Herr, T. et al. Temporal solitons in optical microresonators. *Nat. Photon.* **8**, 145–152 (2013).
This work provides a comprehensive explanation, combining both theory and experiments, of the generation of low-noise soliton mode-locked states that has eluded the community for several years.
192. Yi, X., Yang, Q.-F., Yang, K. Y., Suh, M.-G. & Vahala, K. Soliton frequency comb at microwave rates in a high-Q silica microresonator. *Optica* **2**, 1078 (2015).
193. Gong, Z. et al. High-fidelity cavity soliton generation in crystalline AlN micro-ring resonators. *Opt. Lett.* **43**, 4366–4369 (2018).
194. Pfeiffer, M. H. P. et al. Octave-spanning dissipative Kerr soliton frequency combs in Si_3N_4 microresonators. *Optica* **4**, 684–691 (2017).
195. Joshi, C. et al. Thermally controlled comb generation and soliton modelocking in microresonators. *Opt. Lett.* **41**, 2565 (2016).
This work reports integrated fast tuning of microcombs to mode-locked single-soliton and multisoliton states using integrated platinum microheaters.
196. Liu, J. et al. Monolithic piezoelectric control of soliton microcombs. *Nature* **583**, 385–390 (2020).
197. He, Y. et al. Self-starting bi-chromatic LiNbO3 soliton microcomb. *Optica* **6**, 1138–1144 (2019).
198. Cole, D. C., Lamb, E. S., Del'Haye, P., Diddams, S. A. & Papp, S. B. Soliton crystals in Kerr resonators. *Nat. Photon.* **11**, 671–676 (2017).
199. Corcoran, B. et al. Ultra-dense optical data transmission over standard fibre with a single chip source. *Nat. Commun.* **11**, 2568 (2020).
200. Wilson, D. J. et al. Integrated gallium phosphide nonlinear photonics. *Nat. Photon.* **14**, 57–62 (2020).
201. Moille, G. et al. Dissipative Kerr solitons in a III–V microresonator. *Laser Photon. Rev.* **14**, 2000022 (2020).
202. Weng, H. et al. Directly accessing octave-spanning dissipative Kerr soliton frequency combs in an AlN microresonator. *Photon. Res.* **9**, 1351–1357 (2021).
203. Jung, H., Fong, K. Y., Xiong, C. & Tang, H. X. Electrical tuning and switching of an optical frequency comb generated in aluminum nitride microring resonators. *Opt. Lett.* **39**, 84–87 (2014).
204. Wang, C. et al. Monolithic lithium niobate photonic circuits for Kerr frequency comb generation and modulation. *Nat. Commun.* **10**, 978 (2019).
205. Stern, B., Ji, X., Dutt, A. & Lipson, M. Compact narrow-linewidth integrated laser based on a low-loss silicon nitride ring resonator. *Opt. Lett.* **42**, 4541–4544 (2017).
206. Raja, A. S. et al. Electrically pumped photonic integrated soliton microcomb. *Nat. Commun.* **10**, 680 (2019).
207. Shen, B. et al. Integrated turnkey soliton microcombs. *Nature* **582**, 365–369 (2020).
208. Li, Q. et al. Stably accessing octave-spanning microresonator frequency combs in the soliton regime. *Optica* **4**, 193 (2017).
209. Coen, S. & Erkintalo, M. Universal scaling laws of Kerr frequency combs. *Opt. Lett.* **38**, 1790 (2013).
210. Okawachi, Y. et al. Bandwidth shaping of microresonator-based frequency combs via dispersion engineering. *Opt. Lett.* **39**, 3535 (2014).
211. Riemensberger, J. et al. Dispersion engineering of thick high-Q silicon nitride ring-resonators via atomic layer deposition. *Opt. Express* **20**, 27661 (2012).
212. Yao, B. et al. Gate-tunable frequency combs in graphene–nitride microresonators. *Nature* **558**, 410 (2018).
213. Xue, X. et al. Normal-dispersion microcombs enabled by controllable mode interactions. *Laser Photon. Rev.* **9**, L23–L28 (2015).
214. Jang, J. K. et al. Dynamics of mode-coupling-induced microresonator frequency combs in normal dispersion. *Opt. Express* **24**, 28794–28803 (2016).
215. Xue, X., Wang, P.-H., Xuan, Y., Qi, M. & Weiner, A. M. Microresonator Kerr frequency combs with high conversion efficiency. *Laser Photon. Rev.* **11**, 1600276 (2017).
216. Bao, C. et al. Nonlinear conversion efficiency in Kerr frequency comb generation. *Opt. Lett.* **39**, 6126–6129 (2014).
217. Kim, B. Y. et al. Turn-key, high-efficiency Kerr comb source. *Opt. Lett.* **44**, 4475–4478 (2019).
218. Jang, J. K. et al. Conversion efficiency of soliton Kerr combs. *Opt. Lett.* **46**, 3657–3660 (2021).
219. Obrzud, E., Lecomte, S. & Herr, T. Temporal solitons in microresonators driven by optical pulses. *Nat. Photon.* **11**, 600–607 (2017).

220. Xue, X., Zheng, X. & Zhou, B. Super-efficient temporal solitons in mutually coupled optical cavities. *Nat. Photon.* **13**, 616 (2019).
221. Zhao, Y. et al. Visible nonlinear photonics via high-order-mode dispersion engineering. *Optica* **7**, 135–141 (2020).
222. Lee, S. H. et al. Towards visible soliton microcomb generation. *Nat. Commun.* **8**, 1295 (2017).
223. Karpov, M., Pfeiffer, M. H. P., Liu, J., Lukashchuk, A. & Kippenberg, T. J. Photonic chip-based soliton frequency combs covering the biological imaging window. *Nat. Commun.* **9**, 1146 (2018).
224. Yu, S.-P. et al. Tuning Kerr-soliton frequency combs to atomic resonances. *Phys. Rev. Appl.* **11**, 044017 (2019).
225. Luke, K., Okawachi, Y., Lamont, M. R. E., Gaeta, A. L. & Lipson, M. Broadband mid-infrared frequency comb generation in a Si_3N_4 microresonator. *Opt. Lett.* **40**, 4823–4826 (2015).
226. Gong, Z. et al. Soliton microcomb generation at 2 μm in z-cut lithium niobate microring resonators. *Opt. Lett.* **44**, 3182–3185 (2019).
227. Lau, R. K. W., Lamont, M. R. E., Okawachi, Y. & Gaeta, A. L. Effects of multiphoton absorption on parametric comb generation in silicon microresonators. *Opt. Lett.* **40**, 2778–2781 (2015).
228. Hamerly, R., Gray, D., Rogers, C. & Jamshidi, K. Conditions for parametric and free-carrier oscillation in silicon ring cavities. *J. Lightwave Technol.* **36**, 4671–4677 (2018).
229. Kong, D. et al. Super-broadband on-chip continuous spectral translation unlocking coherent optical communications beyond conventional telecom bands. *Nat. Commun.* **13**, 4139 (2022).
230. Huang, S.-W. et al. Globally stable microresonator turing pattern formation for coherent high-power THz radiation on-chip. *Phys. Rev. X* **7**, 041002 (2017).
231. Levy, J. S. et al. High-performance silicon-nitride-based multiple-wavelength source. *IEEE Photon. Technol. Lett.* **24**, 1375–1377 (2012).
232. Jørgensen, A. A. et al. Petabit-per-second data transmission using a chip-scale microcomb ring resonator source. *Nat. Photon.* **16**, 798–802 (2022).
233. Yu, M., Okawachi, Y., Griffith, A. G., Lipson, M. & Gaeta, A. L. Microfluidic mid-infrared spectroscopy via microresonator-based dual-comb source. *Opt. Lett.* **44**, 4259–4262 (2019).
234. Castro-Beltrán, R., Diep, V. M., Soltani, S., Gungor, E. & Armani, A. M. Plasmonically enhanced Kerr frequency combs. *ACS Photon.* **4**, 2828–2834 (2017).
235. Shen, X., Beltran, R. C., Diep, V. M., Soltani, S. & Armani, A. M. Low-threshold parametric oscillation in organically modified microcavities. *Sci. Adv.* **4**, eaao4507 (2018).
236. Ulvila, V., Phillips, C. R., Halonen, L. & Vainio, M. Frequency comb generation by a continuous-wave-pumped optical parametric oscillator based on cascading quadratic nonlinearities. *Opt. Lett.* **38**, 4281–4284 (2013).
237. Leo, F. et al. Walk-off-induced modulation instability, temporal pattern formation, and frequency comb generation in cavity-enhanced second-harmonic generation. *Phys. Rev. Lett.* **116**, 033901 (2016).
238. Roy, A. et al. Temporal walk-off induced dissipative quadratic solitons. *Nat. Photon.* **16**, 162–168 (2022).
239. Liu, M. et al. High-power mid-IR few-cycle frequency comb from quadratic solitons in an optical parametric oscillator. *Laser Photon. Rev.* **16**, 2200453 (2022).
240. O'Brien, J. L., Furusawa, A. & Vučković, J. Photonic quantum technologies. *Nat. Photon.* **3**, 687–695 (2009).
241. Flamini, F., Spagnolo, N. & Sciarrino, F. Photonic quantum information processing: a review. *Rep. Prog. Phys.* **82**, 016001 (2018).
242. Kok, P. et al. Linear optical quantum computing with photonic qubits. *Rev. Mod. Phys.* **79**, 135–174 (2007).
243. Yoshikawa, J. et al. Invited article: generation of one-million-mode continuous-variable cluster state by unlimited time-domain multiplexing. *APL Photon.* **1**, 060801 (2016).
244. Pysher, M., Miwa, Y., Shahrokhshahi, R., Bloomer, R. & Pfister, O. Parallel generation of quadripartite cluster entanglement in the optical frequency comb. *Phys. Rev. Lett.* **107**, 030505 (2011).
245. Takeda, S. & Furusawa, A. Toward large-scale fault-tolerant universal photonic quantum computing. *APL Photon.* **4**, 060902 (2019).
246. Wang, J. et al. Multidimensional quantum entanglement with large-scale integrated optics. *Science* **360**, 285–291 (2018).
In this paper, multidimensional quantum entanglement is realized by integrating up to 16 silicon spontaneous four-wave mixing sources with reconfigurable beam splitters and waveguide crossings on a single chip.
247. Caspani, L. et al. Integrated sources of photon quantum states based on nonlinear optics. *Light Sci. Appl.* **6**, e17100 (2017).
248. Spring, J. B. et al. Chip-based array of near-identical, pure, heralded single-photon sources. *Optica* **4**, 90–96 (2017).
249. Dutt, A. et al. On-chip optical squeezing. *Phys. Rev. Appl.* **3**, 044005 (2015).
This paper reports the first nanophotonic quantum-squeezed light source, that is, all-optical squeezed light generation using a high-confinement platform.
250. Braunstein, S. L. & van Loock, P. Quantum information with continuous variables. *Rev. Mod. Phys.* **77**, 513–577 (2005).
251. Andersen, U. L., Gehring, T., Marquardt, C. & Leuchs, G. 30 years of squeezed light generation. *Phys. Scr.* **91**, 053001 (2016).
252. Mohanty, A. et al. Quantum interference between transverse spatial waveguide modes. *Nat. Commun.* **8**, 14010 (2017).
253. Taballione, C. et al. 8×8 reconfigurable quantum photonic processor based on silicon nitride waveguides. *Opt. Express* **27**, 26842–26857 (2019).
254. Somaschi, N. et al. Near-optimal single-photon sources in the solid state. *Nat. Photon.* **10**, 340–345 (2016).
255. Aharonovich, I., Englund, D. & Toth, M. Solid-state single-photon emitters. *Nat. Photon.* **10**, 631–641 (2016).
256. Azzini, S. et al. Ultra-low power generation of twin photons in a compact silicon ring resonator. *Opt. Express* **20**, 23100–23107 (2012).
257. Guo, X. et al. Parametric down-conversion photon-pair source on a nanophotonic chip. *Light Sci. Appl.* **6**, e16249 (2017).
258. Alibart, O. et al. Quantum photonics at telecom wavelengths based on lithium niobate waveguides. *J. Opt.* **18**, 104001 (2016).
259. Sanaka, K., Kawahara, K. & Kuga, T. New high-efficiency source of photon pairs for engineering quantum entanglement. *Phys. Rev. Lett.* **86**, 5620–5623 (2001).
260. Tanzilli, S. et al. Highly efficient photon-pair source using periodically poled lithium niobate waveguide. *Electron. Lett.* **37**, 26–28 (2001).
261. Förtsch, M. et al. A versatile source of single photons for quantum information processing. *Nat. Commun.* **4**, 1818 (2013).
262. Lanco, L. et al. Semiconductor waveguide source of counterpropagating twin photons. *Phys. Rev. Lett.* **97**, 173901 (2006).
263. Autebert, C. et al. Integrated AlGaAs source of highly indistinguishable and energy-time entangled photons. *Optica* **3**, 143–146 (2016).
264. Jin, H. et al. On-chip generation and manipulation of entangled photons based on reconfigurable lithium-niobate waveguide circuits. *Phys. Rev. Lett.* **113**, 103601 (2014).
265. Luo, R. et al. On-chip second-harmonic generation and broadband parametric down-conversion in a lithium niobate microresonator. *Opt. Express* **25**, 24531 (2017).
266. Xin, C. J. et al. Spectrally separable photon-pair generation in dispersion engineered thin-film lithium niobate. *Opt. Lett.* **47**, 2830–2833 (2022).
267. Dalidet, R. et al. Near perfect two-photon interference out of a down-converter on a silicon photonic chip. *Opt. Express* **30**, 11298–11305 (2022).
268. Clemmen, S. et al. Continuous wave photon pair generation in silicon-on-insulator waveguides and ring resonators. *Opt. Express* **17**, 16558–16570 (2009).
269. Sharping, J. E. et al. Generation of correlated photons in nanoscale silicon waveguides. *Opt. Express* **14**, 12388 (2006).
270. Takesue, H. et al. Generation of polarization entangled photon pairs using silicon wire waveguide. *Opt. Express* **16**, 5721–5727 (2008).
271. Gentry, C. M. et al. Quantum-correlated photon pairs generated in a commercial 45 nm complementary metal-oxide semiconductor microelectronic chip. *Optica* **2**, 1065–1071 (2015).
272. Spring, J. B. et al. On-chip low loss heralded source of pure single photons. *Opt. Express* **21**, 13522–13532 (2013).
273. Yan, Z. et al. Generation of heralded single photons beyond 1100 nm by spontaneous four-wave mixing in a side-stressed femtosecond laser-written waveguide. *Appl. Phys. Lett.* **107**, 231106 (2015).
274. Imany, P. et al. 50-GHz-spaced comb of high-dimensional frequency-bin entangled photons from an on-chip silicon nitride microresonator. *Opt. Express* **26**, 1825–1840 (2018).
275. Ramelow, S. et al. Silicon-nitride platform for narrowband entangled photon generation. Preprint at https://arxiv.org/abs/1508.04358 (2015).
276. Samara, F. et al. High-rate photon pairs and sequential time-bin entanglement with Si_3N_4 microring resonators. *Opt. Express* **27**, 19309–19318 (2019).
277. Lu, X. et al. Chip-integrated visible–telecom entangled photon pair source for quantum communication. *Nat. Phys.* **15**, 373–381 (2019).
278. Collins, M. J. et al. Low Raman-noise correlated photon-pair generation in a dispersion-engineered chalcogenide As_2S_3 planar waveguide. *Opt. Lett.* **37**, 3393–3395 (2012).
279. Sangouard, N., Simon, C., de Riedmatten, H. & Gisin, N. Quantum repeaters based on atomic ensembles and linear optics. *Rev. Mod. Phys.* **83**, 33–80 (2011).
280. Vanselow, A., Kaufmann, P., Chrzanowski, H. M. & Ramelow, S. Ultra-broadband SPDC for spectrally far separated photon pairs. *Opt. Lett.* **44**, 4638 (2019).
281. Harris, N. C. et al. Integrated source of spectrally filtered correlated photons for large-scale quantum photonic systems. *Phys. Rev. X* **4**, 041047 (2014).
282. Davanço, M. et al. Telecommunications-band heralded single photons from a silicon nanophotonic chip. *Appl. Phys. Lett.* **100**, 261104 (2012).
283. Xiong, C. et al. Slow-light enhanced correlated photon pair generation in a silicon photonic crystal waveguide. *Opt. Lett.* **36**, 3413–3415 (2011).
284. Silverstone, J. W. et al. On-chip quantum interference between silicon photon-pair sources. *Nat. Photon.* **8**, 104–108 (2014).
285. Silverstone, J. W. et al. Qubit entanglement between ring-resonator photon-pair sources on a silicon chip. *Nat. Commun.* **6**, 7948 (2015).
286. Preble, S. F. et al. On-chip quantum interference from a single silicon ring-resonator source. *Phys. Rev. Appl.* **4**, 021001 (2015).
287. Qiang, X. et al. Large-scale silicon quantum photonics implementing arbitrary two-qubit processing. *Nat. Photon.* **12**, 534–539 (2018).
288. Kues, M. et al. Quantum optical microcombs. *Nat. Photon.* **13**, 170–179 (2019).
289. Reimer, C. et al. High-dimensional one-way quantum processing implemented on *d*-level cluster states. *Nat. Phys.* **15**, 148 (2019).
290. Xie, Z. et al. Harnessing high-dimensional hyperentanglement through a biphoton frequency comb. *Nat. Photon.* **9**, 536–542 (2015).
291. Javid, U. A. et al. Chip-scale simulations in a quantum-correlated synthetic space. *Nat. Photon.* **17**, 883–890 (2023).

292. Jiang, W. C., Lu, X., Zhang, J., Painter, O. & Lin, Q. Silicon-chip source of bright photon pairs. *Opt. Express* **23**, 20884–20904 (2015).
293. Joshi, C. et al. Frequency-domain quantum interference with correlated photons from an integrated microresonator. *Phys. Rev. Lett.* **124**, 143601 (2020).
294. Wang, X.-L. et al. 18-qubit entanglement with six photons' three degrees of freedom. *Phys. Rev. Lett.* **120**, 260502 (2018).
295. Feng, L.-T. et al. On-chip transverse-mode entangled photon pair source. *npj Quantum Inf.* **5**, 1–7 (2019).
296. Christ, A. & Silberhorn, C. Limits on the deterministic creation of pure single-photon states using parametric down-conversion. *Phys. Rev. A* **85**, 023829 (2012).
297. Migdall, A. L., Branning, D. & Castelletto, S. Tailoring single-photon and multiphoton probabilities of a single-photon on-demand source. *Phys. Rev. A* **66**, 053805 (2002).
298. Mower, J. & Englund, D. Efficient generation of single and entangled photons on a silicon photonic integrated chip. *Phys. Rev. A* **84**, 052326 (2011).
299. Ma, X., Zotter, S., Kofler, J., Jennewein, T. & Zeilinger, A. Experimental generation of single photons via active multiplexing. *Phys. Rev. A* **83**, 043814 (2011).
300. Xiong, C. et al. Active temporal multiplexing of indistinguishable heralded single photons. *Nat. Commun.* **7**, 10853 (2016).
301. Menicucci, N. C. Fault-tolerant measurement-based quantum computing with continuous-variable cluster states. *Phys. Rev. Lett.* **112**, 120504 (2014).
302. Fukui, K., Tomita, A., Okamoto, A. & Fujii, K. High-threshold fault-tolerant quantum computation with analog quantum error correction. *Phys. Rev. X* **8**, 021054 (2018).
303. Huh, J., Guerreschi, G. G., Peropadre, B., McClean, J. R. & Aspuru-Guzik, A. Boson sampling for molecular vibronic spectra. *Nat. Photon.* **9**, 615–620 (2015).
304. Lvovsky, A. I. in *Photonics* Ch. 5 (ed. Andrews, D. L.) 121–163 (John Wiley & Sons, Ltd, 2015).
305. Giovannetti, V., Lloyd, S. & Maccone, L. Quantum-enhanced measurements: beating the standard quantum limit. *Science* **306**, 1330–1336 (2004).
306. Aasi, J. et al. Enhanced sensitivity of the LIGO gravitational wave detector by using squeezed states of light. *Nat. Photon.* **7**, 613–619 (2013).
307. Taylor, M. A. et al. Biological measurement beyond the quantum limit. *Nat. Photon.* **7**, 229–233 (2013).
308. Stokowski, H. S. et al. Integrated quantum optical phase sensor in thin film lithium niobate. *Nat. Commun.* **14**, 3355 (2023).
309. Fürst, J. U. et al. Quantum light from a whispering-gallery-mode disk resonator. *Phys. Rev. Lett.* **106**, 113901 (2011).
310. Otterpohl, A. et al. Squeezed vacuum states from a whispering gallery mode resonator. *Optica* **6**, 1375 (2019).
311. Bergman, K., Haus, H. A., Ippen, E. P. & Shirasaki, M. Squeezing in a fiber interferometer with a gigahertz pump. *Opt. Lett.* **19**, 290–292 (1994).
312. Cernansky, R. & Politi, A. Nanophotonic source of broadband quadrature squeezing. *APL Photonics* **5**, 101303 (2020).
313. Ast, S. et al. Continuous-wave nonclassical light with gigahertz squeezing bandwidth. *Opt. Lett.* **37**, 2367–2369 (2012).
314. Silberhorn, C., Korolkova, N. & Leuchs, G. Quantum key distribution with bright entangled beams. *Phys. Rev. Lett.* **88**, 167902 (2002).
315. Lenzini, F. et al. Integrated photonic platform for quantum information with continuous variables. *Sci. Adv.* **4**, eaat9331 (2018).
316. Khorasani, S. Third-order optical nonlinearity in two-dimensional transition metal dichalcogenides. *Commun. Theor. Phys.* **70**, 344 (2018).
317. Vahlbruch, H., Mehmet, M., Danzmann, K. & Schnabel, R. Detection of 15 dB squeezed states of light and their application for the absolute calibration of photoelectric quantum efficiency. *Phys. Rev. Lett.* **117**, 110801 (2016).
318. Yoshino, K., Aoki, T. & Furusawa, A. Generation of continuous-wave broadband entangled beams using periodically poled lithium niobate waveguides. *Appl. Phys. Lett.* **90**, 041111 (2007).
319. Kanter, G. et al. Squeezing in a $LiNbO_3$ integrated optical waveguide circuit. *Opt. Express* **10**, 177 (2002).
320. Stefszky, M. et al. Waveguide cavity resonator as a source of optical squeezing. *Phys. Rev. Appl.* **7**, 044026 (2017).
321. Pysher, M. et al. Broadband amplitude squeezing in a periodically poled $KTiOPO_4$ waveguide. *Opt. Lett.* **34**, 256–258 (2009).
322. Eto, Y. et al. Efficient homodyne measurement of picosecond squeezed pulses with pulse shaping technique. *Opt. Lett.* **36**, 4653–4655 (2011).
323. Dutt, A. et al. Tunable squeezing using coupled ring resonators on a silicon nitride chip. *Opt. Lett.* **41**, 223 (2016).
324. Vaidya, V. D. et al. Broadband quadrature-squeezed vacuum and nonclassical photon number correlations from a nanophotonic device. *Sci. Adv.* **6**, eaba9186 (2020).
325. Hoff, U. B., Nielsen, B. M. & Andersen, U. L. Integrated source of broadband quadrature squeezed light. *Opt. Express* **23**, 12013–12036 (2015).
326. Zhao, Y. et al. Near-degenerate quadrature-squeezed vacuum generation on a silicon-nitride chip. *Phys. Rev. Lett.* **124**, 193601 (2020).
327. Zhang, Y. et al. Squeezed light from a nanophotonic molecule. *Nat. Commun.* https://doi.org/10.1038/s41467-021-22540-2 (2021).
328. Arrazola, J. M. et al. Quantum circuits with many photons on a programmable nanophotonic chip. *Nature* **591**, 54–60 (2021).
329. Gottesman, D. & Preskill, J. in *Quantum Information with Continuous Variables* (eds Braunstein, S. L. & Pati, A. K.) 317–356 (Springer Netherlands, 2003).
330. Roslund, J., de Araújo, R. M., Jiang, S., Fabre, C. & Treps, N. Wavelength-multiplexed quantum networks with ultrafast frequency combs. *Nat. Photon.* **8**, 109–112 (2014).
331. Chen, M., Menicucci, N. C. & Pfister, O. Experimental realization of multipartite entanglement of 60 modes of a quantum optical frequency comb. *Phys. Rev. Lett.* **112**, 120505 (2014).
332. Yang, Z. et al. A squeezed quantum microcomb on a chip. *Nat. Commun.* **12**, 4781 (2021).
333. Chen, P.-K., Chen, P.-K., Briggs, I., Hou, S. & Fan, L. Ultra-broadband quadrature squeezing with thin-film lithium niobate nanophotonics. *Opt. Lett.* **47**, 1506–1509 (2022).
334. Nehra, R. et al. Few-cycle vacuum squeezing in nanophotonics. *Science* **377**, eabo6213 (2022).
This paper reports the first squeezing in thin-film lithium niobate, measured over a broad wavelength range using phase-sensitive optical parametric amplification.
335. Knill, E., Laflamme, R. & Milburn, G. J. A scheme for efficient quantum computation with linear optics. *Nature* **409**, 46 (2001).
336. Raussendorf, R. & Briegel, H. J. A one-way quantum computer. *Phys. Rev. Lett.* **86**, 5188–5191 (2001).
337. Bartolucci, S. et al. Fusion-based quantum computation. *Nat. Commun.* **14**, 912 (2023).
338. Pant, M., Towsley, D., Englund, D. & Guha, S. Percolation thresholds for photonic quantum computing. *Nat. Commun.* **10**, 1070 (2019).
339. Li, Y., Humphreys, P. C., Mendoza, G. J. & Benjamin, S. C. Resource costs for fault-tolerant linear optical quantum computing. *Phys. Rev. X* **5**, 041007 (2015).
340. Langford, N. K. et al. Efficient quantum computing using coherent photon conversion. *Nature* **478**, 360–363 (2011).
341. Yanagimoto, R., Ng, E., Jankowski, M., Mabuchi, H. & Hamerly, R. Temporal trapping: a route to strong coupling and deterministic optical quantum computation. *Optica* **9**, 1289 (2022).
342. Yanagimoto, R. et al. Quantum nondemolition measurements with optical parametric amplifiers for ultrafast universal quantum information processing. *PRX Quantum* **4**, 010333 (2023).
343. Krastanov, S. et al. Room-temperature photonic logical qubits via second-order nonlinearities. *Nat. Commun.* **12**, 191 (2021).
344. Heuck, M., Jacobs, K. & Englund, D. R. Controlled-phase gate using dynamically coupled cavities and optical nonlinearities. *Phys. Rev. Lett.* **124**, 160501 (2020).
345. Li, M. et al. Photon–photon quantum phase gate in a photonic molecule with $\chi^{(2)}$ nonlinearity. *Phys. Rev. Appl.* **13**, 044013 (2020).
346. Chang, D. E., Douglas, J. S., González-Tudela, A., Hung, C.-L. & Kimble, H. J. Colloquium: quantum matter built from nanoscopic lattices of atoms and photons. *Rev. Mod. Phys.* **90**, 031002 (2018).
347. Venkataraman, V., Saha, K. & Gaeta, A. L. Phase modulation at the few-photon level for weak-nonlinearity-based quantum computing. *Nat. Photon.* **7**, 138–141 (2013).
348. Peyronel, T. et al. Quantum nonlinear optics with single photons enabled by strongly interacting atoms. *Nature* **488**, 57–60 (2012).
349. Chang, D. E., Vuletić, V. & Lukin, M. D. Quantum nonlinear optics — photon by photon. *Nat. Photon.* **8**, 685–694 (2014).
350. Chang, T.-H., Fields, B. M., Kim, M. E. & Hung, C.-L. Microring resonators on a suspended membrane circuit for atom–light interactions. *Optica* **6**, 1203–1210 (2019).
351. Yang, K. Y. et al. Inverse-designed non-reciprocal pulse router for chip-based LiDAR. *Nat. Photon.* **14**, 369–374 (2020).
352. Hughes, T. W., Minkov, M., Williamson, I. A. D. & Fan, S. Adjoint method and inverse design for nonlinear nanophotonic devices. *ACS Photon.* **5**, 4781–4787 (2018).
353. Smirnova, D., Leykam, D., Chong, Y. & Kivshar, Y. Nonlinear topological photonics. *Appl. Phys. Rev.* **7**, 021306 (2020).
354. Carletti, L., Koshelev, K., De Angelis, C. & Kivshar, Y. Giant nonlinear response at the nanoscale driven by bound states in the continuum. *Phys. Rev. Lett.* **121**, 033903 (2018).
355. Wang, J. et al. Doubly resonant second-harmonic generation of a vortex beam from a bound state in the continuum. *Optica* **7**, 1126–1132 (2020).
356. Okawachi, Y. et al. Demonstration of chip-based coupled degenerate optical parametric oscillators for realizing a nanophotonic spin-glass. *Nat. Commun.* **11**, 4119 (2020).
357. Ji, X. et al. Exploiting ultralow loss multimode waveguides for broadband frequency combs. *Laser Photon. Rev.* **15**, 2000353 (2021).
358. Cardenas, J. et al. High Q SiC microresonators. *Opt. Express* **21**, 16882–16887 (2013).
359. Yu, M., Desiatov, B., Okawachi, Y., Gaeta, A. L. & Lončar, M. Coherent two-octave-spanning supercontinuum generation in lithium-niobate waveguides. *Opt. Lett.* **44**, 1222–1225 (2019).
360. Liu, X. et al. Integrated continuous-wave aluminum nitride Raman laser. *Optica* **4**, 893–896 (2017).
361. He, Y., Liang, H., Luo, R., Li, M. & Lin, Q. Dispersion engineered high quality lithium niobate microring resonators. *Opt. Express* **26**, 16315–16322 (2018).
362. Miller, S. A. et al. Tunable frequency combs based on dual microring resonators. *Opt. Express* **23**, 21527 (2015).
363. Soltani, M., Matsko, A. & Maleki, L. Enabling arbitrary wavelength frequency combs on chip. *Laser Photon. Rev.* **10**, 158–162 (2016).
364. Lu, J. et al. Periodically poled thin-film lithium niobate microring resonators with a second-harmonic generation efficiency of 250,000%/W. *Optica* **6**, 1455–1460 (2019).
365. Xiong, C. et al. Quantum-correlated photon pair generation in chalcogenide As_2S_3 waveguides. *Opt. Express* **18**, 16206–16216 (2010).
366. Mendoza, G. J. et al. Active temporal and spatial multiplexing of photons. *Optica* **3**, 127–132 (2016).

367. Savchenkov, A. A. et al. Tunable optical frequency comb with a crystalline whispering gallery mode resonator. *Phys. Rev. Lett.* **101**, 093902 (2008).
368. Telle, H. R. et al. Carrier-envelope offset phase control: a novel concept for absolute optical frequency measurement and ultrashort pulse generation. *Appl. Phys. B* **69**, 327–332 (1999).
369. Foster, M. A., Moll, K. D. & Gaeta, A. L. Optimal waveguide dimensions for nonlinear interactions. *Opt. Express* **12**, 2880–2887 (2004).
370. Koos, C., Jacome, L., Poulton, C., Leuthold, J. & Freude, W. Nonlinear silicon-on-insulator waveguides for all-optical signal processing. *Opt. Express* **15**, 5976–5990 (2007).
371. Lacava, C., Pusino, V., Minzioni, P., Sorel, M. & Cristiani, I. Nonlinear properties of AlGaAs waveguides in continuous wave operation regime. *Opt. Express* **22**, 5291–5298 (2014).
372. Kuyken, B. et al. Nonlinear properties of and nonlinear processing in hydrogenated amorphous silicon waveguides. *Opt. Express* **19**, B146–B153 (2011).
373. Turner, A. C. et al. Tailored anomalous group-velocity dispersion in silicon channel waveguides. *Opt. Express* **14**, 4357–4362 (2006).
374. Domeneguetti, R. R. et al. Parametric sideband generation in CMOS-compatible oscillators from visible to telecom wavelengths. *Optica* **8**, 316–322 (2021).
375. Ramelow, S. et al. Strong polarization mode coupling in microresonators. *Opt. Lett.* **39**, 5134 (2014).
376. Mia, M. B., Jaidye, N. & Kim, S. Extremely high dispersions in heterogeneously coupled waveguides. *Opt. Express* **27**, 10426–10437 (2019).
377. Alexander, K., Savostianova, N. A., Mikhailov, S. A., Kuyken, B. & Van Thourhout, D. Electrically tunable optical nonlinearity of graphene-covered SiN waveguides. *ACS Photonics* **4**, 3039–3044 (2017).
378. Yuan, Z. et al. Soliton pulse pairs at multiple colours in normal dispersion microresonators. *Nat. Photon.* **17**, 977–983 (2023).
379. Lu, X., Rao, A., Moille, G., Westly, D. A. & Srinivasan, K. Universal frequency engineering tool for microcavity nonlinear optics: multiple selective mode splitting of whispering-gallery resonances. *Photon. Res.* **8**, 1676–1686 (2020).
380. McGarvey-Lechable, K. & Bianucci, P. Maximizing slow-light enhancement in one-dimensional photonic crystal ring resonators. *Opt. Express* **22**, 26032–26041 (2014).
381. Yu, S.-P., Lucas, E., Zang, J. & Papp, S. B. A continuum of bright and dark-pulse states in a photonic-crystal resonator. *Nat. Commun.* **13**, 3134 (2022).
382. Marty, G., Combrié, S., Raineri, F. & De Rossi, A. Photonic crystal optical parametric oscillator. *Nat. Photon.* **15**, 53–58 (2021).

Acknowledgements
The authors thank C. Joshi for fruitful discussions. A.D. was supported by seed grants from Northrop Grumman and NAWCAD (Grant no. N004212310002). A.M. is supported by the Henry Luce Foundation through the Clare Boothe Luce Program.

Author contributions
A.D. and A.M. researched data for the article. All authors contributed substantially to discussion of the content. All authors wrote the article. All authors reviewed and/or edited the manuscript before submission.

Competing interests
The authors declare no competing interests.

Additional information
Peer review information *Nature Reviews Materials* thanks David Moss for their contribution to the peer review of this work.

Publisher's note Springer Nature remains neutral with regard to jurisdictional claims in published maps and institutional affiliations.